Centre for Geo-Information

Thesis Report GIRS-2006-04

Spatial estimation of Digital Surface Model generation errors via digital photogrammetry.

Itay Bar-on

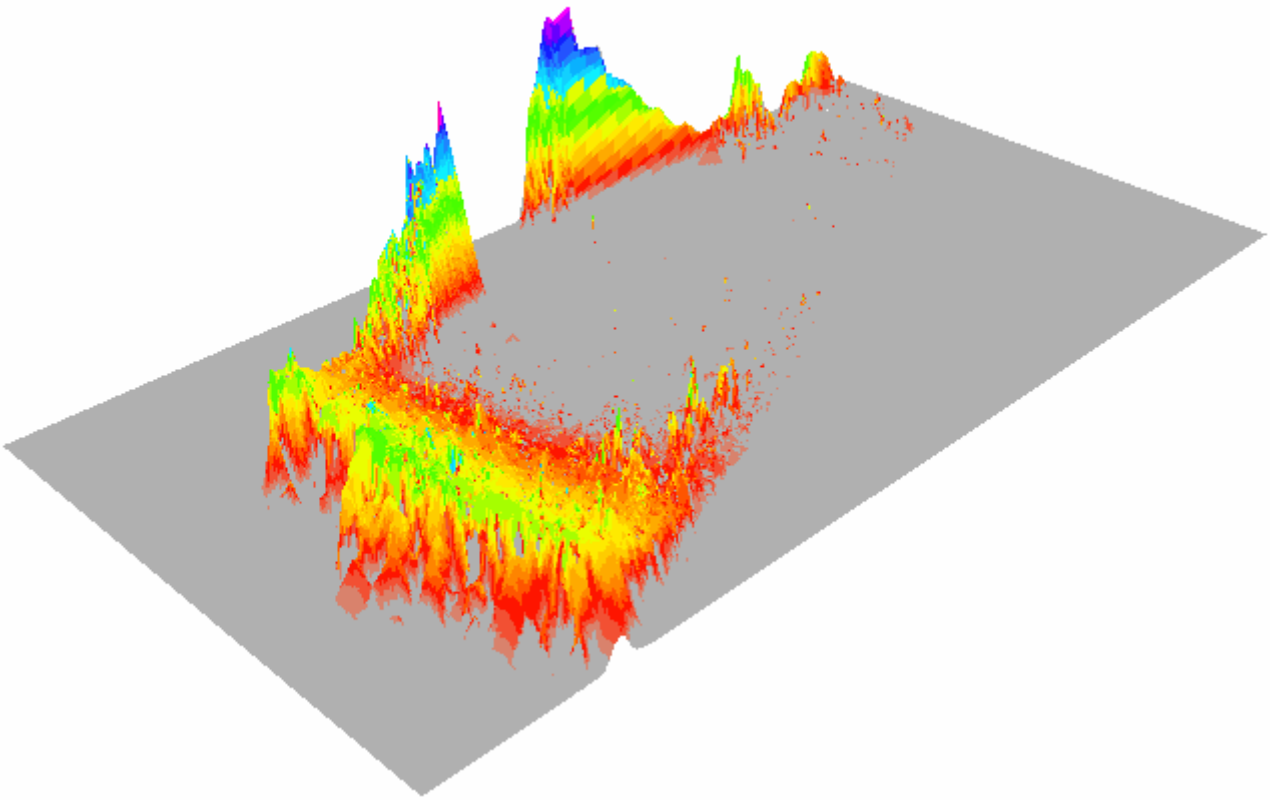

WAGENINGEN UNIVERSITY
WAGENINGEN UR

Spatial estimation of Digital Surface Model generation errors via digital photogrammetry.

Itay Bar-on

Registration number 7507034120

Supervisors:

Bartholomeus, Harm

Stuiver, John

Centre for Geo-Information (CGI), Wageningen, The Netherlands.

A thesis submitted in partial fulfilment of the degree of Master of Science
at Wageningen University and Research Centre,
The Netherlands.

February 2006

Wageningen, The Netherlands

Thesis code number: GRS-80436
Thesis Report: GIRS-2006-04
Wageningen University and Research Centre
Centre for Geo-Information

Acknowledgements.

The following research could not have possibly be the same without the patience and professional knowledge of my supervisors Harm Bartholomeus and John Stuiver. In addition, Mr. Janhein Loedeman is thanked for his enthusiasm and devotion to the research and Mr. Philip Wenting for the technical support.

Table of contents.

List of tables.

List of figures.

Abstract.

The research provides insights to a new photogrammetric approach that deals with the quality of Digital Surface Model (DSM) generation, spatially. With the use of Leica Photogrammetry Suite (LPS) software module, aerial triangulation was preformed twice. First, with two high-resolution aerial images (UltraCam images) and secondly with orthoimages produced from the first aerial triangulation. For the generated DSM's, validation took place by means of Differential GPS (DGPS) point analysis and by generating an orthoDSM (DSM from orthoimages). Furthermore, the DSM generated from the best image layer is used to estimate and compare forest volume with conventional forestry measurements.

The main results indicate that an overestimation of heights takes place when generating a DSM and there are significant differences when using default or expert DSM generation settings. The main research conclusions are that the DSM validation should not be done by the internal validation procedure. The potential to estimate spatially DSM generation errors, with the orthoDSM generation and the significance of Ground Control Points (GCP's) distribution in the DSM generation are shown. Further research and improvements should take place to develop a fully functional and adaptive spatial DSM error estimation tool.

1 Introduction and Background.

1.1 Introduction.

The following pages present the research problem definition, objective and research questions.

1.1.1 Problem definition.

Ongoing international concern about the effects of increased atmospheric concentrations of greenhouse gases (CO_2, CH_4, N_2O, HFC, PFC's and SF_6) on the global climate system resulted in adoption of the UN Framework Convention on climate changes in 1992 (Adapted from the United Nations Framework convention on climate change 1992). Despite its promising start, it proves to be difficult to realize. None the less, Article 4.1(d) of the Convention committed parties to 'promote sustainable management and promote and cooperate in the conservation and enhancement as appropriate, of sinks and reservoirs of greenhouse gases not controlled by the Montreal Protocol, including biomass, forests, oceans and other terrestrial coastal and marine ecosystems' (Adapted from the United Nations Framework convention on climate change 1992).
The capabilities of vegetation to use and fixate carbon dioxide (CO_2) through the process of photosynthesis are a well-known fact.
Aerial and satellite imagery provide the possibilities to obtain high levels of spatial detail and temporal sequences necessary to assess vegetation changes and characteristics. Detection of vegetation changes and occurrences by means of aerial photographs and satellite imagery has been addressed by many with different approaches (Brown and Carter, 1998; Goslee et al., 2003; Hudak and Wessman, 2001). The quantification of vegetation using aerial or satellite images has also been a subject given much attention.(Couteron, 2002; Elmore et al., 2000; Laliberte et al., 2004). The current possibilities provided by high resolution digital aerial photographs and high resolution satellite imagery to gather accurate assessments of vegetation characteristics contributes to the enhancement of managing, monitoring and detecting changes in vegetation (Mucher, 2003).
Accurate measurements concerning vegetation biomass and vegetation changes relates directly to Article 4.1(d) of the Kyoto Convention, that promotes sustainable management of terrestrial and marine ecosystems.
Despite advances in combining multiple data sources such as Airborne Laser Scanning (ALS) with aerial photographs (Suarez et al., 2005), 3D GIS (Vosselman et al., 2005), image segmentation methods (Schiewe, 2003; Vosselman et al., 2005) and surface clustering (Filin, 2004) these methodologies are in the development and testing phase. Baltsavias (2004) summarizes image analysis trends, strategies and system aspects of knowledge-based image analysis. The potential embedded in multi-sensor systems, has been currently applied almost entirely for fabricated objects (buildings and roads). Other objects (vegetation, crops and wetlands) receive a smaller amount of attention from the scientific and commercial sectors.
In the forestry sector the use of different data sources (conventional inventory plot data in combination with aerial or satellite imagery) to obtain accurate forest parameters (height, volume, forest health) has a long history (Holmgren, 1998).

In the context of this research accurate quantitative scene interpretation is defined as adequate interpretation of multiple-images that leads to accurate forest volume estimation.
Further research into accurate quantitative forest parameters estimation should take place, because of continuous demand from the scientific and commercial sectors for improvement (Hyvonen et al., 2005) and since it will enhance the information available to forest managers and owners and therefore can contribute to sustainable forest management and monitoring.

1.1.2 Research objective.

The objective of this research is to explore the possibilities of estimating forest volume by generating a Digital Surface Model (DSM) from digital aerial photographs (UltraCam images).

1.1.3 Research questions.

The following paragraph present the research questions dealt with in the course of the research.

1. Can accurate DSM's be generated from high-resolution digital aerial photographs (UltraCam images) to assist in forest volume estimation?

    1.1. What are the accuracies of the default generated DSM's?
    1.2. Do other DSM generation settings improve the DSM's accuracies?
    1.3. Are there differences in the DSM's accuracies when using different image layers for the DSM's generations?
    1.4. Does the possibility to correct the DSM's, in a single-step, exist?
    1.5. Are there accuracy differences between the photogrammetric generated DSM's and the ALS produced DSM (AHN DSM)?

2. Can accurate forest volume estimation be made from the generated DSM and UltraCam image?.

    2.1 How accurate are the volumes estimated from the image and generated DSM, in comparison with volumes estimated by conventional forestry volume measurements?

1.2 Background.

The subject of digital photogrammetry its methods, main processes, terminology and its uses within forestry are introduced.

1.2.1 Photogrammetry.

The word “Photogrammetry” is derived from three Greek words, *photos* meaning “light”, *gramma* meaning “something drawn or written” and *metron* meaning “to measure.” The root words, therefore, originally signified measuring graphically by means of light.

Photogrammetry is the "art, science and technology of obtaining reliable information about physical objects and the environment through the process of recording, measuring and interpreting photographic images and patterns of electromagnetic radiant imagery and other phenomena" (ASP, 1980).

Photogrammetry is considered to be invented in 1851 by Laussedat. Over time, the development of photogrammetry has passed through the phases of Plane Table Photogrammetry, Analogue Photogrammetry, Analytical Photogrammetry, and has recently entered the phase of Digital Photogrammetry (Konecny, 1994).

Digital Photogrammetry is photogrammetry as applied to digital images that are stored and processed on a computer. Some Photogrammetric tasks can be (semi)automated in digital photogrammetry (e.g., automatic DEM generation and digital orthoimage generation).

1.2.2 Use of photogrammetry in forestry.

Photogrammetric interpretation of qualitative and quantitative forest stand characteristics using manual methods of stereo photogrammetry has been studied widely since 1940 (Korpela, 2004). More recently automated and semi automated methods for tree or stand interpretation have evolved with the development of digital photogrammetry, which has its roots in computer technology, digital image analysis and analytical photogrammetry.

Aerial imagery may be more useful than satellite images because of their higher spatial resolution, as this will improve the classification of forest stands and provide estimates of stand characteristics commonly required in forestry inventory (Wulder and Franklin, 2003).

Aerial photographs have been and continue to be the most frequently used remote sensing data source in forestry, particularly in natural resource assessment, inventory and monitoring (Caylor, 2000; Gillis and Leckie, 1993; Hall and Fent, 1996).

According to Hyvonen (2005) several studies that used digital analysis of very high spatial resolution (VHR) images to produce information for forest inventory and management have been published (e.g. Anttila, 2002; Tuominen et al., 2003). According to these studies, the use of VHR imagery provides a better basis for remote sensing-aided forest management planning than the high-resolution (e.g. Landsat TM) satellite images. However, the use of VHR data sources requires different approaches to feature generation and image analysis in general.

1.2.3 Individual tree feature extraction.

Forest management stands usually consist of several tree species, which may be situated unevenly within the stand. Thus, the stand characteristics and stand-level features only offer an average description of the stand. To obtain accurate information, the units of data collection and feature generation should be more homogeneous.

This issue has provided the background for algorithms and methods development of individual tree feature generation (Culvenor, 2002; Gougeon, 1999; Korpela, 2004; Leckie et al., 2003; Pekkarinen, 2002; Wulder et al., 2000) and the establishment of the International Forum on Automated Interpretation of High Spatial Resolution Digital for Forestry, in 1999. In this forum investigations on individual crown detection took place with the use of high-resolution imagery. International and national pressures to ensure sustainable forest management are resulting in fine mapping stands attributes such as stand volume, stem density, gap size and distribution. Generating tree and stand attributes from VHR imagery is an approach that can complement existing inventory data acquisition programs (Wulder and Franklin, 2003). Furthermore, much attention is given to the potentials embedded in LIDAR technology to map forest attributes (Andersen et al., 2005; Bortolot and Wynne, 2005; Hudak et al., 2002; Kraus and Pfeifer, 1998; Lefsky et al., 1999; Maltamo et al., 2004; Nilsson, 1996; Suarez et al., 2005; Zimble et al., 2003) and hyperspectral images (Blackburn, 2002; Greenberg et al., 2005) as complementary technologies to be integrated with known digital photogrammetry methods and forest inventory methods.

1.2.4 Terminology.

The more important research terms are defined and presented.

The U.S. Geological Survey defines a Digital Elevation Model (DEM) as the digital cartographic representation of the terrain at regularly spaced intervals in X and Y directions using Z values referenced to a common vertical datum.

A Digital Terrain Model (DTM) is used in some countries as a synonym for DEM, but a DTM can also include the elevation of important topographic features on land, mass points and break lines to better characterize the bare earth terrain.

A Digital Surface Model (DSM) represents the elevation of the top surfaces of buildings, trees and other features elevated above bare ground, which is the difference of DSM from DEM or DTM. In this research, the term DSM is used as a synonym for DTM.

An orthoDSM is a DSM generated from orthoimages. The values of the orthoDSM do not represent height, but a spatial indication of DSM generation errors.

Best image layer is defined as a spectral image layer, which is has the highest probability of accurate representation the terrain feature's heights.

The definition of a Ground Control Point (GCP) is a point in the terrain of known, or accurately determined horizontal and vertical positions.

The GCP is inserted into the images and gains; also, the image's coordinates system. Therefore, a GCP has two sets of coordinate systems (i.e. terrain X, Y, Z and image x, y, respectively).

A checkpoint definition is a point in the terrain of known, or accurately determined horizontal and vertical positions. It is used only to check the coordinate transformation accuracies.
A tie point is an image point, identified on overlapping images. They serve to tie individual images into a network of images (block). Tie points have image coordinates and after determination through photogrammetric methods, they are transformed into terrain coordinates.

1.2.5 Aerial Triangulation.

Aerial triangulation (AT) is a well-established procedure for obtaining the exterior and interior orientation parameters for a set of aerial photographs. It is the first and most critical step of photogrammetric processing. The main purpose is to orient every stereo model using GCP's.
One of the major tasks in aerial triangulation is the measurement of conjugate points on two or more partially overlapping photographs (image matching). Schenk (1997) presents a review concerning automatic and interactive aerial triangulation methods, main tasks involved in automatic aerial triangulation and problems encountered with aerial triangulation products (DEM and orthoimages).
Since the basis of this research rests on the image-matching method used, an introduction and description of the subject is given.

1.2.6 Image matching.

One of the most fundamental process in photogrammetry is to identify and to measure conjugate points in two or more overlapping photographs (Schenk, 1999). Digital image matching can be defined as "automatically establishing the correspondence between primitives generated from two or more images depicting at least partly the same scene" (Heipke, 1996).
Using different image-matching methods, many tasks in digital photogrammetry are carried out automatically, such as; interior orientation, relative orientation, point transfer in aerial triangulation, absolute orientation and DEM generation (Ackermann and Krzystek, 1991; Forstner, 1995; Heipke, 1996; Heipke, 1997; Schenk, 1996).
Image matching has a long history, with the first experiments starting in the fifties (Hobrough, 1959). In the early seventies until the mid- eighties, research related to image matching focused on digital correlation techniques (Helava, 1978; Hobrough, 1978; Kreiling, 1976).
The complex task of locating conjugate points on different images, a task easily done by humans, was underestimated and lead to little results. For the last two decades, the advancements in computer vision and a better understanding of human vision have lead to improvements in image-matching methods.
The best-known matching methods are described in table 1. The first column lists the matching methods; the second (similarity measure) is a quantitative measure of correspondence between two conjugate features or points (cost function relates to a correlation coefficient limit). The last column refer to the image primitive being compared, primitives include grey levels, generated features and symbolic descriptions. The area - based matching will be discussed in more detail because of its application in this research. A more detailed overview concerning feature and symbolic matching methods is given by Schenk (1999).

Table 1: Image matching methods.

Matching methods	Similarity measure	Matching entities
Area - based	Correlation, least - squares	Grey levels
Feature - based	Cost function	Edges, regions
Symbolic	Cost function	Symbolic description

Area - based matching is associated with matching grey levels, meaning the grey level distribution of small areas of two images (image patches) are compared and the similarity is measured by correlation or least-squares techniques.
The idea behind Least-Squares Matching (LSM) is to minimize the grey level differences between the search window and the correlation window First results from experiments with LSM were reported in the early eighties by Ackermann (1984); Grun (1985); Grun and Baltsavias (1987); Forstner (1995; 1982); Rosenholm (1987); Thurgood and Mikhail (1982).
In Forstner (1984), the author assesses the quality of image correlation techniques. In addition, Schenk (1999) provides a detailed description of LSM.
In this research the area-based matching method with a least - squares approach for measuring similarity (least - squares matching: LSM) is used.

1.2.7 Camera positioning data.

Nowadays with the integration of Global Positioning System (GPS), Inertial Navigation Systems (INS) , Inertial Measurement Unit (IMU) and digital aerial cameras (Burtch, 2000; Cramer and Stallmann, 2001; Ebadi, 1997; Ip, 2005; Wang et al., 2003), GPS-aided navigation, direct georeferencing and locating the position of sensor during exposure (exposure centres) can be accurately defined (Mostafa and Hutton, 2005).

1.2.8 DSM generation.

After the orientation of the stereo model, the DSM generation can take place. (Yastikli and Jacobsen) (2005) provide an overview about automatic DEM generation, problems and restrictions. Interpolation procedures are addressed by (Schmidt) (2001), DEM determination by (Trinder) (2002) and an integration of multi-data approach is presented by Schiewe (2003).
There are significant consequences to the choice made concerning the DSM output format. The output format can have a profound effect on the reliability and precision of the DSM and is usually application specific. In this research, the Raster and ASCII file formats will be used.

1.2.9 Orthorectification.

Orthorectification takes a raw digital image and applies an elevation model (DSM) and triangulation results to create an orthoimage (digital orthoimage).
An image or photograph with an orthographic projection is one for which every point looks as if an observer were looking straight down at it, along a line of sight that is orthogonal (perpendicular) to the earth.

2 Materials and data.

2.1 The UltraCam – D.

The UltraCam - D is a large format digital Aerial camera system produced by Vexcel. More detail information regarding the camera is found in www.vexcel.com.

2.1.1 UltraCam images.

The two Colour Infra Red (CIR) images used in this research are acquired by Aerodata International Surveys at August 2004.
The images format is TIFF with an 8-bit radiometric resolution. The spatial resolution is of 0.25m per pixel, there are 11500 pixels wide and 7500 high, which returns an approximate area of 5.4 square kilometres. The image scale is approximately 1:27,500. The main image layers characteristics are presented in Table 2. With the images, also the camera calibration report is supplied. This report contains information regarding the camera properties (focal length, radial lens distortion) and information regarding the camera's calibration process.

Table 2: Statistics of image layers based on Digital Numbers (DN).

Image 33 layer	Green	Red	NIR
STDEV	38.8	39.9	28.3
Mean	101.7	111.1	168.8
Median	91.2	99.8	172.6
Mode	83.3	82.0	177.6
Range	1-255	1-254	1-255
Image 34 layer	Green	Red	NIR
STDEV	49.0	47.7	31.9
Mean	115.0	123.3	173.4
Median	98.0	110.0	176.0
Mode	81.0	80.0	181.0
Range	1-255	1-255	1-255

2.2 AHN: Actual Height model of the Netherlands.

The AHN is an elevation model of the Netherlands made by means of ALS. The (unfiltered) point data, representing the top of vegetation and buildings (AHN DSM) is used in the DSM validation, to verify the AHN DSM accuracy.
For more information about the AHN, visit the AHN website (www.ahn.nl).

2.3 Study area.

The study area is a small forest patch (ca. 3.5 ha) located at the “De Born” university complex, Wageningen. The location of the study area is presented at figure 1.
For the digital representation of the study area, the TOP10 vector dataset was used.

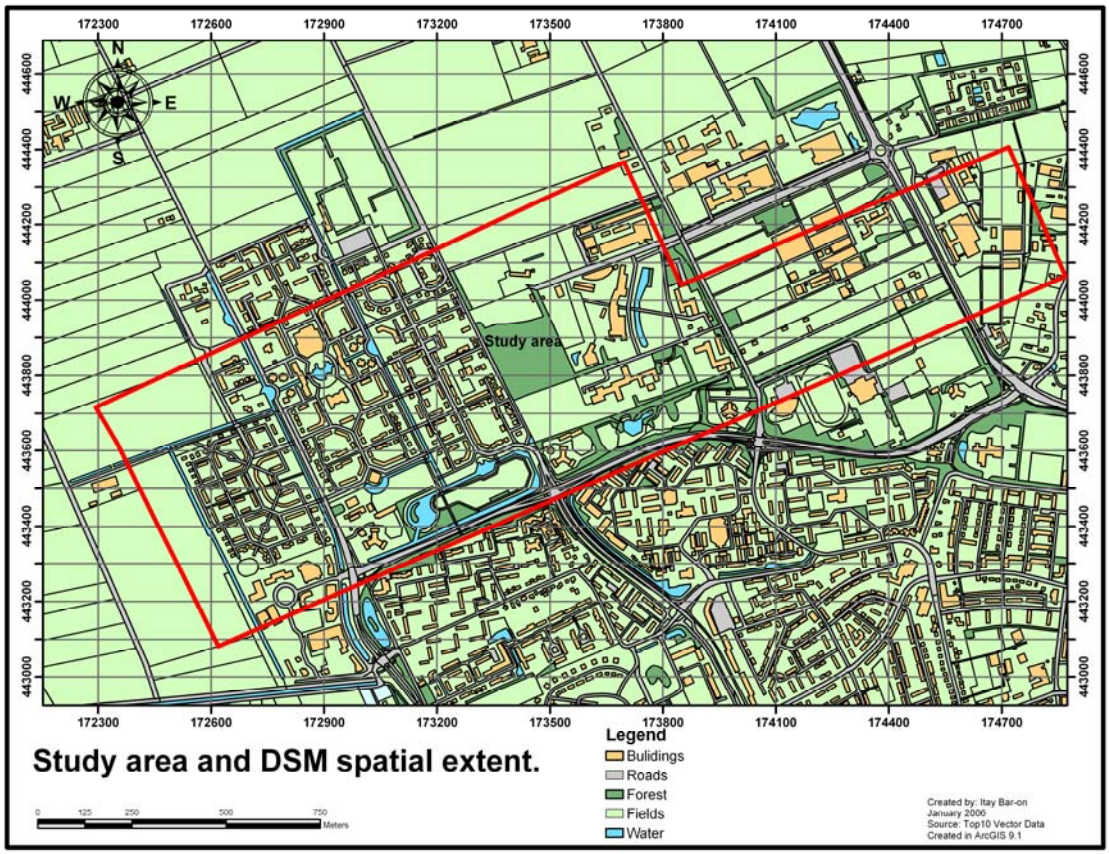

Fig. 1: Study area location and DSM spatial extent indicated by red line.

2.4 Software.

The photogrammetric methods in this research were carried out using the Leica Photogrammetry Suite (LPS) module from the Erdas Imagine 8.7 software package. ArcGIS 9.1 of ESRI, MS office Excel 2003 and SPSS 12.0.1 were used for the DSM's analysis and forest volume estimation and comparison.
For the estimation of forest volume, a SPSS forest inventory module was used (FEM-22306 course material).
eCogition 4.0 of Definiens was used for the DSM and image segmentation trials.
Chartist 4.2b by Novagraph was used for creating the methodology flowcharts and MS Paint 5.1 was used for image editing and conversion.

3 Methodology.

3.1 Creating research products.

The processes creating the research products are presented and described in the following pages. Table 3 presents the estimated number of GCP sets needed and their use. The need for more than one GCP set come from the difference in DSM and orthoDSM extents and the fact that once orthoimages are produced the image coordinate of the first GCP set change into estimated terrain coordinates.
Sets C and D are needed to demonstrate the effect of GCP distribution.

Table 3: Estimated GCP sets and their use.

GCP set	A	B	C	D
Image layer	G/R/NIR	Best	Best	Best
Output	DSM	OrthoDSM	OrthoDSM	OrthoDSM
Purpose	DSM generation, sensitivity analysis	OrthoDSM generation	GCP distribution influence	GCP distribution influence

3.1.1 GCP's measurements.

All GCP's sets and independent checkpoints measurements were carried out using a Real Time Kinetics (RTK) measurements with a Trimble (4700) GPS receiver, Trimble dual frequency L1/L2 antenna and a TSC field computer. Average instrument accuracies are reported to be 1-2 cm horizontal accuracy and 3-5 cm vertical accuracy. Independent control points, used only for the DSM's validation, were collected by mounting the DGPS antenna on a bicycle. The measurements were taken on roads and bike paths in the study vicinity (more detailed information concerning the locations of these points are in appendix C).

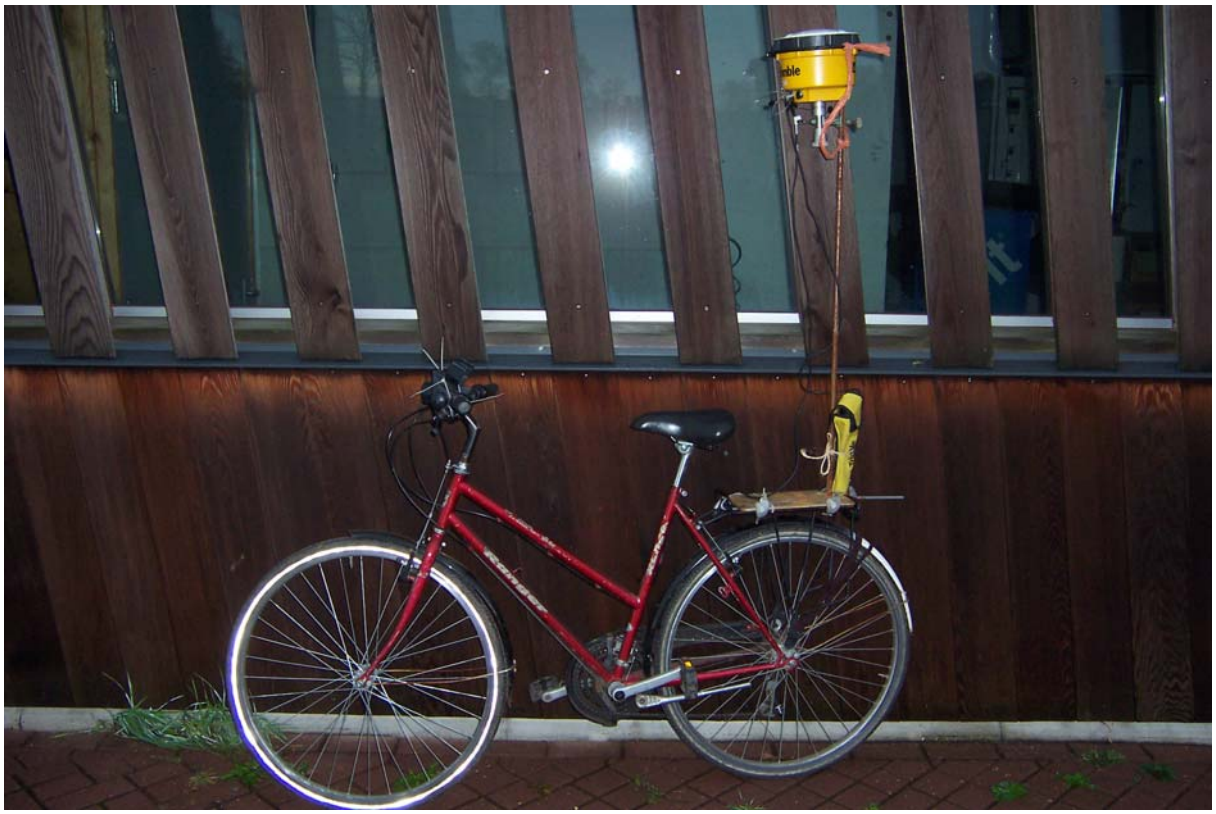

Fig. 2: DGPS bike used to measure independent control points.

3.1.2 Aerial Triangulation.

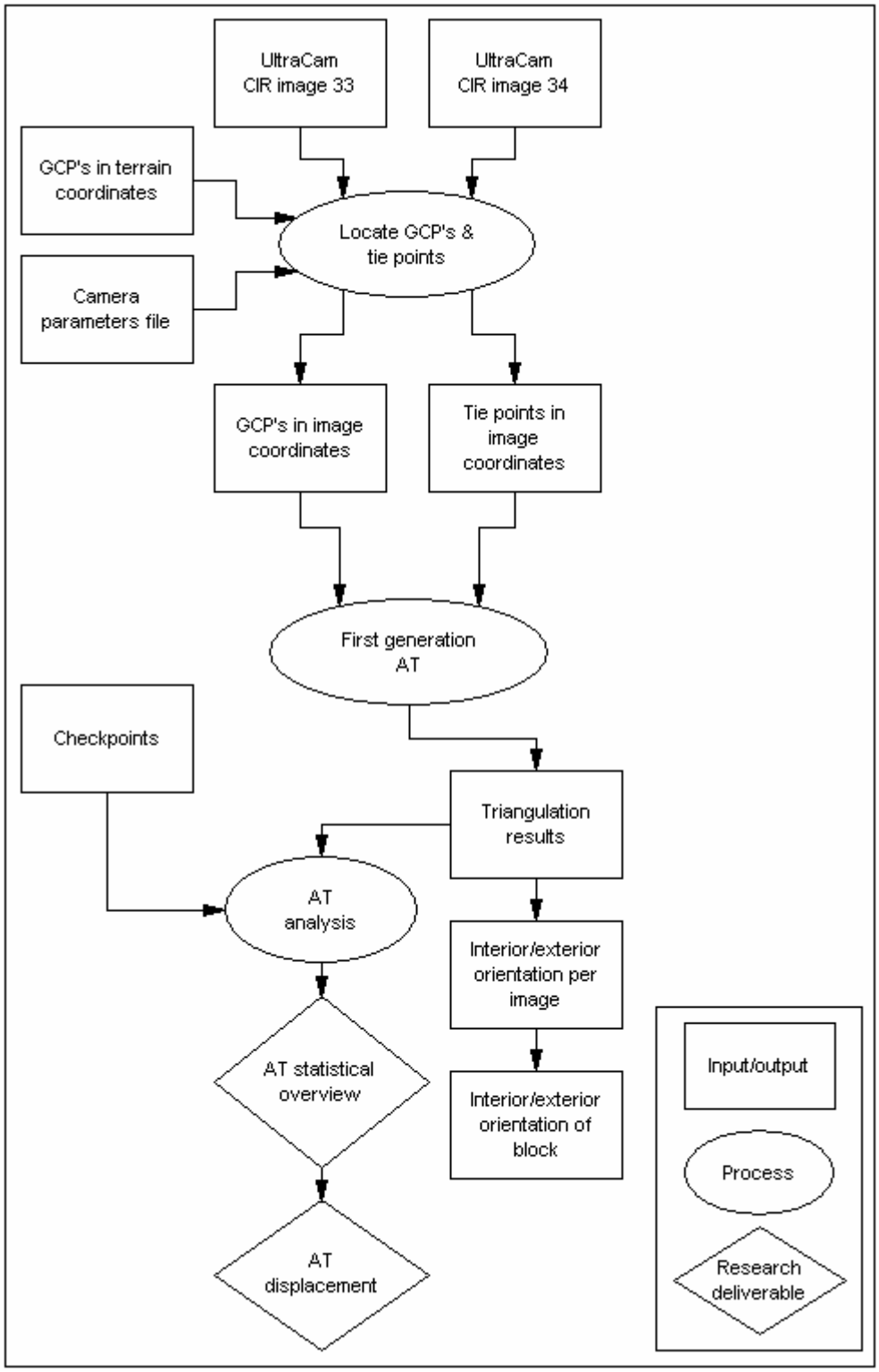

Fig. 3: Flowchart aerial triangulation.

The concept of AT was introduced in paragraph (1.2.5) of the background and introduction chapter. Figure 2 presents the general process of AT.

In the course of this research AT takes place twice:
First, to determine the DSM and orthoimages. (First generation AT)
In a later stage AT is used to get a spatial estimation of DSM error locations. (Second generation AT).
There is a clear distinction between the first generation and second generation AT. In the first generation AT, the original aerial images and all relevant camera information (radial lens distortion and focal length) are used. After the first triangulation, the lens distortion is removed and therefore it is necessary not to use the lens distortion before the second generation AT, with the orthoimages takes place.

The AT process starts with the input of tie points and GCP's. In this research, the Exterior Orientation (EO) of the camera had to be computed, since the supplied EO was incomplete. Once the GCP's and tie points are known in the image coordinate system the aerial triangulation can take place. This results in computation of the interior and exterior model parameters for each image and for the entire block. A statistical indicator (RMSE) that defines the degree of correspondence between the computed locations and the original locations is displayed. A low value indicates better results. Finally the quality of the triangulation results are verified by means of independent checkpoints, in the AT analysis.
An acceptable AT result relay on the rules of thumbs stating that the X and Y precision is 0.01% of the flight height (in this case around 0.3m) and the Z precision is 0.03% of the flight height (i.e. 0.9m).

Simply put an acceptable AT has an accuracy of total RMSE < 1 pixel and checkpoints and GCP's Z values < 0.9m.

In this research the AT statistical overview is not only composed of the total RMSE but also the GCP's and checkpoints RMSE of the Z-axis are added. The addition of these values is based on the facts that these values are most sensitive to relief displacement, image tilt and XY parallax and therefore are best indicators of heights accuracies.

3.1.3 DSM and orthoimages generation.

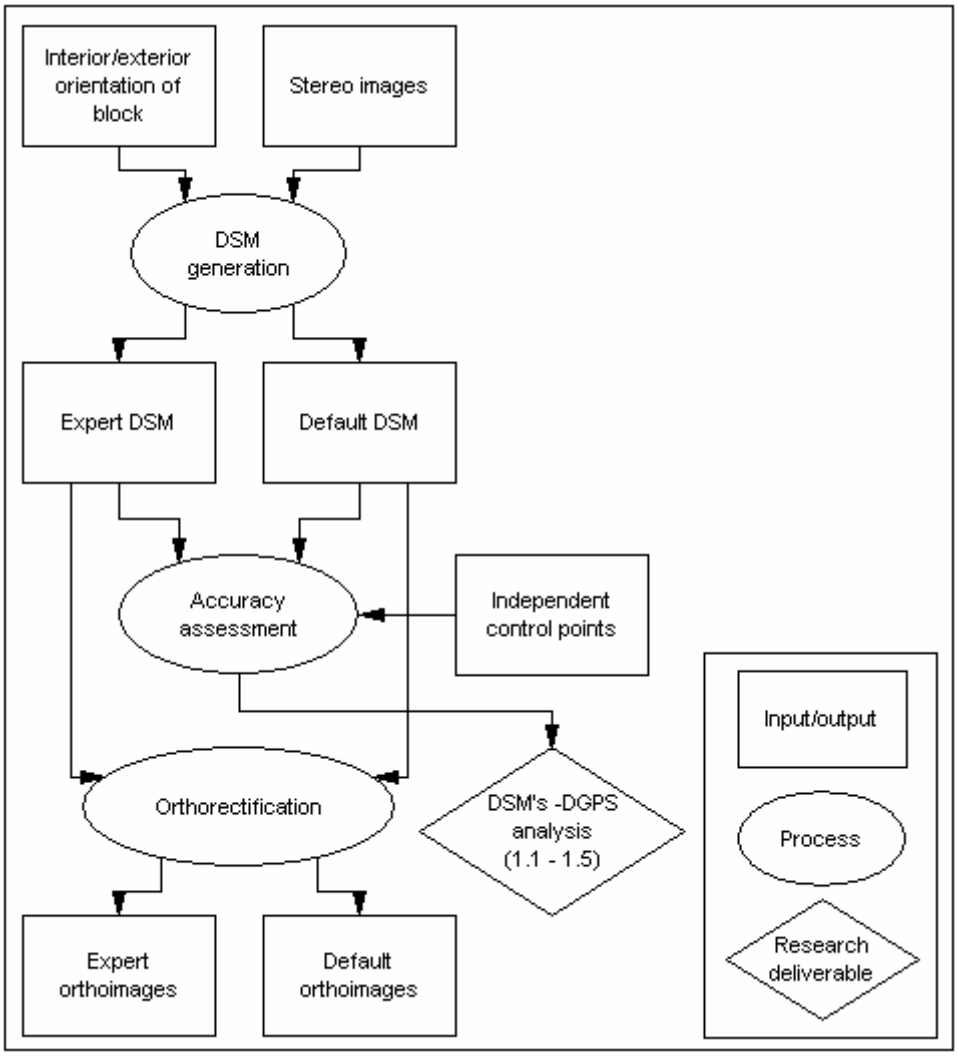

Fig. 4: Flowchart DSM and orthoimages generation numbers in parentheses refer to research questions and sub-research questions.

The block parameters (interior and exterior parameters) along with known points in the terrain coordinates are used together with the stereo image pairs to generate the DSM's. The generated DSM's are an input in the orthorectification process.
The following settings were applied in all DSM generations.

- Trimming of 5% of the borders,
- 3 X 3 meter DSM cell size,
- Horizontal units set to meters,
- Vertical units set to centimetres,
- A single DSM mosaic,
- Pixels are made square.

Two different settings are used for DSM's generation: the default settings and expert settings. The choice to generate the DSM's in two different ways was taken to investigate whether the expert DSM generation settings and derived product (expert DSM) deliver better results than default settings. The following paragraph describes the method used to establish the expert DSM generation settings.

Both the default and expert DSM's were used in the orthoimages generation. It was decided to use the default re-sampling setting (bilinear) since the effect of the re-sampling method was negligible due to the DSM's extent. More information concerning the orthorectification settings are in appendix J.

3.1.4 Sensitivity analysis (Expert DSM generation settings).

The method used to define the expert settings was by using an internal validation procedure (i.e. "DTM Point Status Image") which is a classification of the DSM cell's height presented as a thematic image depicting five classes of correlation. The correlation can take place with the block GCP's, checkpoints or tie points height values and the estimated DSM cell height values. Only the block's checkpoints are used in the internal validation correlation because the GCP's are already involved in the AT process and should not be used for the validation. The tie points are not reliable enough to be used. The checkpoints are not used in the coordinate system transformation only to check the accuracy of that transformation. More information regarding the classification process is in appendix E.

Three DSM generation settings were analyzed: Search window size, correlation window size and coefficient limit. This is done since they are the most important and influential settings. It was decided not to use the adaptive window possibilities because of the unclear processes behind this setting.

The definition of the expert DSM generation settings was done as follows:
1. The process started by running the DSM generation on default settings. A "DTM Point Status Image" was created for the default DSM.
2. Next step was to change only one parameter (for example the X value for the search window, the rest of settings is left on default) and generate a DSM with these settings. A "DTM Point Status Image" was created for the corresponding DSM and the correlated points with excellent value (representing a 0.85 to 1 correlation) were plotted. The X and Y search windows would be limited because of the large number of sizes available. The testing of the coefficient limit was restricted to maximum 0.95 to avoid applying a high constrain on the correlation. All the available window sizes for the correlation window were tested.
3. In the case that no definite generation setting could be defined, the setting before the default setting was used. This was done to confine and restrict the expert generation settings. After defining all the expert generation settings, the expert DSM generation took place.
4. For the expert and default DSM's a "DTM Point Status Image" was generated, to visualize the possible improvements of the expert DSM generation settings and to check the validity of the internal validation process with the independent DSM validation.

3.2 Validation.

The methods used for the research validation are presented in the next pages.

3.2.1 Aerial Triangulation displacement.

In order to assess wheatear the accuracy of the AT process is within acceptable tolerances (2-3 pixels = 0.5-0.75 m) the GCP's location, measured with DGPS, was compared to the estimated location resulting from the AT. This was done by using most of the DGPS measured GCP's as tie points in the AT. This way the displacements could be analysed, since only tie points coordinates (image coordinates) transform into terrain coordinates.

3.2.2 DSM accuracies with independent DGPS measurements.

independent control points are used DSM-DGPS analysis. The DGPS points were measured with the same equipment and accuracies as the GCP's used in the AT. To select the appropriate DSM's points corresponding with the DGPS points the following steps were taken:

1. All DSM's were generated as ASCII point data format.
2. A selection of DGPS points that are within the DSM's extent was carried out.
3. A buffer of 1m was set up around the selected DGPS points, a smaller buffer proved to be inadequate, since only a very few DSM's points were selected.
4. An intersection of the 1m buffer with the DSM's points was made. This resulted in a combined feature class containing the attributes of the defaults and experts DSM's point data and the DGPS point data.
5. The DGPS Z values were plotted in such a way that a 1 to 1 line resulted and the selected defaults and experts DSM's Z values, were plotted on the Y (with corresponding DGPS points on the X-axis).

An investigation to determine if underestimation or overestimation of the DSM's heights took place. The following steps describe the method applied:

1. A new column was added to the feature classes containing both DSM's and DGPS heights (previous step 4).
2. The result of subtracting the DGPS heights from the DSM's heights was introduced into the new column.
3. A classification of the heights differences took place.
4. A spatial representation of the heights differences was carried out.

3.2.3 Spatial estimation of DSM generation errors.

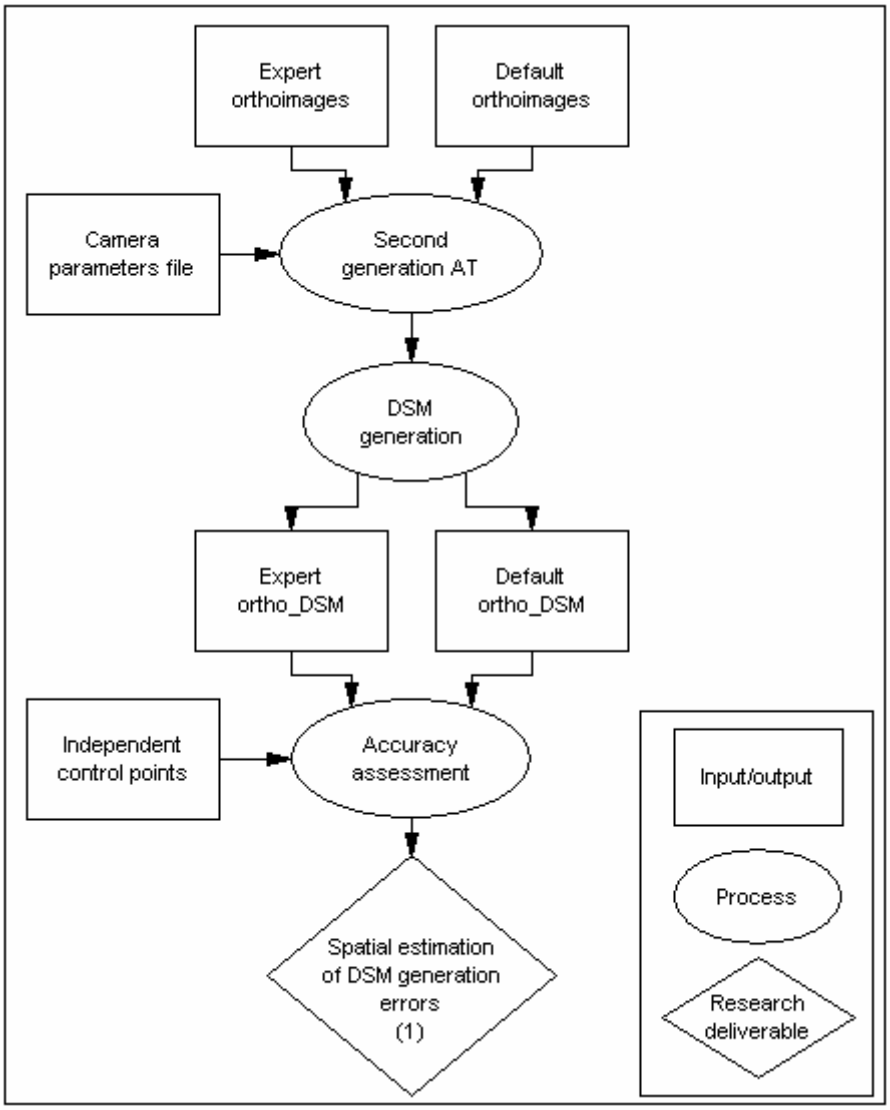

Fig. 5: Flowchart Spatial estimation of DSM error locations numbers in parentheses refer to research questions and sub-research questions.

The spatial estimation of DSM generation errors takes place by means of a second generation AT. The second generation AT was done with best image layer and a DSM (orthoDSM) was generated from the orthoimages using the default and expert DSM generation settings. The resulting orthoDSM's should principally be completely flat, since orthoimages are, free of image tilt and relief displacement.
These properties of orthoimages provide the opportunity to investigate, surface wise, the reliability of the DSM generation process and provide a spatial estimation of the image matching and DSM generation errors.

In addition, the distribution of GCP's and its effect on the DSM generation was investigated. This was done by performing AT and generating an orthoDSM with three GCP's and afterwards adding one GCP to the existing block GCP's and generating a second orthoDSM.

3.3 Application.

Presented are the research application's methods. In order to answer the second research question a characterisation of the study area's specie composition and tree volume was carried out. Furthermore, segmentation trials with the best image layer DSM and image were done. The characterisation of the study area along with the DSM and image segmentation trials, are attempts to narrow the gap between Remote Sensing (RS) measurements and conventional forestry measurements.

3.3.1 Field data collection.

The study area's species composition was established by inventorying three circular sampling plots, with the 21-trees sampling method (FEM-22306 course material). Considering the heterogeneous nature of the study area, three sampling plots were sufficient to estimate the tree volume with a high degree of confidence in the measurements. Each tree in the sample plots was measured for its diameter with a measuring tape. The individual tree height was established by measuring the tree height from two sides using a clinometer (Forester vertex type of Haglof). The data was processed further to compute the study area tree volume and derivatives.

3.3.2 Segmentation trials.

All segmentation trials were preformed using the eCognition software. The best image layer DSM and image segmentation trials were done to reduce the total estimated study area volume to an estimated tree volume. All segmentation trials were done with the default segmentation settings, with variations in the segmentation ´scale´ and the inclusion/exclusion of the DSM and image in the segmentation process.

3.3.3 Volume comparison.

The estimation of tree volume, derived from DSM/image segmentation, is done by multiplying the number of estimated trees in the study area with the average tree specie volume in the study area. A comparison is carried out between the estimated tree volume via conventional forestry measurements and tree volume derived from RS measurements.

4 Results and Discussion.

The main research results are presented and discussed.

4.1 Research products.

The following pages present the research results of the research products, followed by a discussion extending on the implications, contradictions and relevance for the products results.

4.1.1 GCP's measurements.

The following figure and table are the results of the GCP's measurements. GCP's and checkpoints collection took place on the 7th and 14th of September 2005. The locations of the checkpoints can be found in appendix C.

Table 4: GCP's measurements.

GCP set	A	B	C	D
Image layer	G/R/NIR	NIR	NIR	NIR
GCP number	3	5	3	4
Output	DSM	OrthoDSM	OrthoDSM	OrthoDSM
Purpose	DSM generation, sensitivity analysis	OrthoDSM generation	GCP distribution influence	GCP distribution influence

Detailed GCP's location are given in appendix A.

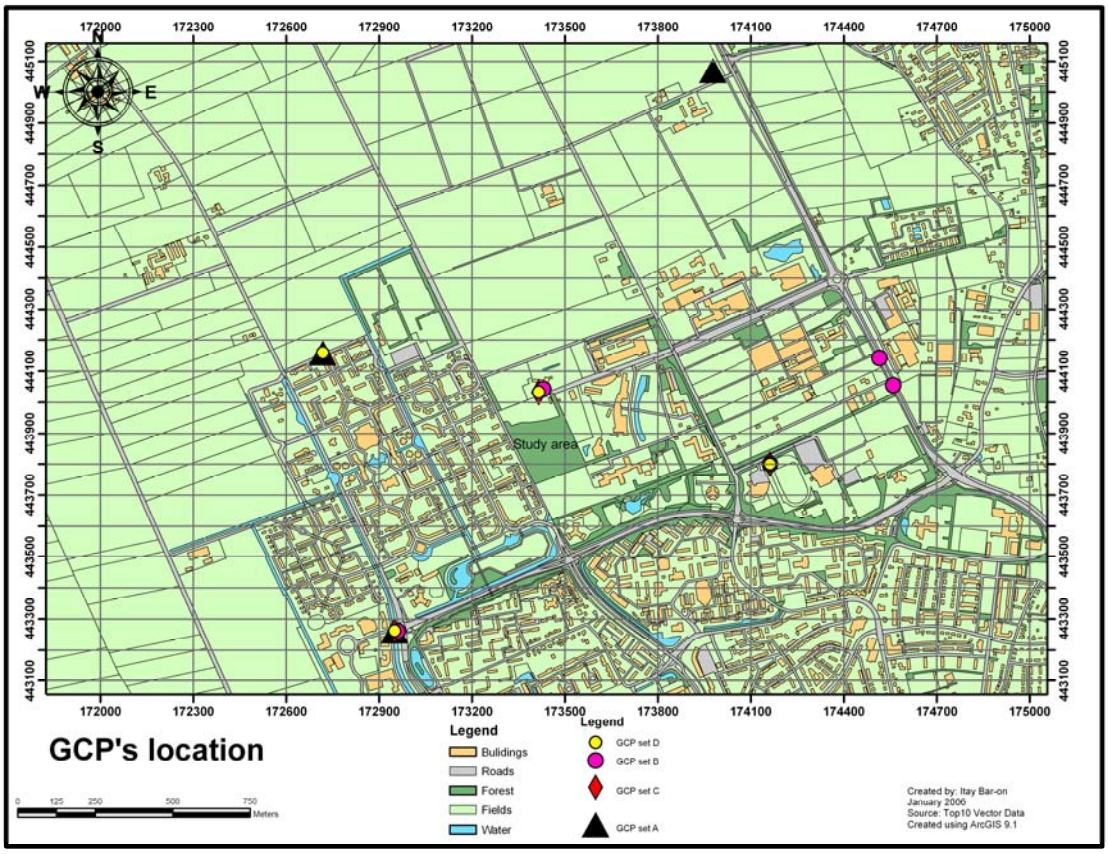

Fig. 6: GCP's location in RD coordinates.

4.1.2 Aerial Triangulation.

The obtained AT results are presented and discussed.
The results obtained in the first generation AT are accepted, not only because of the acceptable triangulation summery information (figure 7), but mainly because of the independent validation of these results by means of investigating the AT displacement (4.2.1). The result of the second generation AT, with the orthoimages, is definitely questionable. However, the interpretation of this triangulation summary should be done with caution due to the uncertain AT summery units. In the first AT summary the units of the check and control points RMSE are meters, in the second generation AT the orthoimages units are the coordinate system (RD). The AT summary units are of unknown value and this could accounts for the large control points and checkpoints RMSE. Detailed information concerning the AT results are in appendix D.

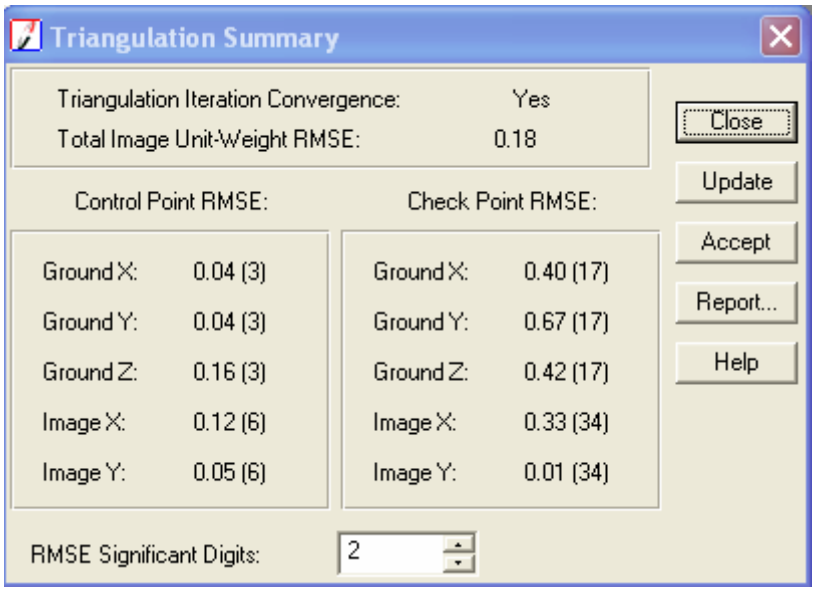

Fig. 7: First generation AT results.

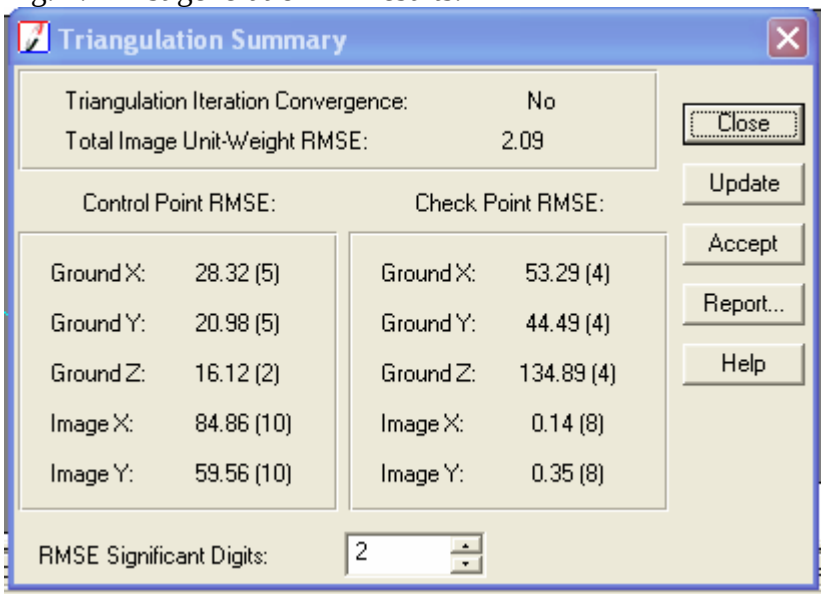

Fig. 8: Second generation AT results.

4.1.3 DSM's.

Presented are some images and results of the DSM generation.
There are significant differences in the number of DSM points between the DSM's generated from the different image layers (Table 5). Especially in the spatial extent of the study area, a large difference exists. This is because the NIR image layer contains a large range of grey scale levels (texture) and, therefore, more correlated height points are found. There are also differences, but not as big, between the numbers of DSM points generated using default and expert DSM generation settings. The significance of the spectral information used through photogrammetric methods should not be ignored. Nevertheless, with the rise of new technologies the use of photogrammetric methods to extract accurate DSM's, hangs in question. The potential of Light Detection and Ranging (LIDAR) technology to model real world surfaces, with a high degree of accuracy, has made its first tentative steps into the commercial sector in the past few years. According to current commercial sensor development, the synergy between sensors is already taking place.
In the academic sector, with its more tentative approach to new technologies, a broad range of LIDAR related research is taking place. From visualising urban features (Priestnall, 2000), measuring ocean waves (Hwang et al., 2000) to forestry and environmental monitoring (Hudak et al., 2002; Lefsky et al., 1999; Maltamo et al., 2004; Nilsson, 1996; Rango et al., 2000; Zimble et al., 2003).
Baltsavias (1999) compares ALS with photogrammetry, where he states possible points of advantage ALS has over photogrammetry and vice versa and concludes that the technologies support and balance each other rather than replace each other. The science of photogrammetry with its long history of methods and technological development can still provide valuable information through the spectral properties of images.

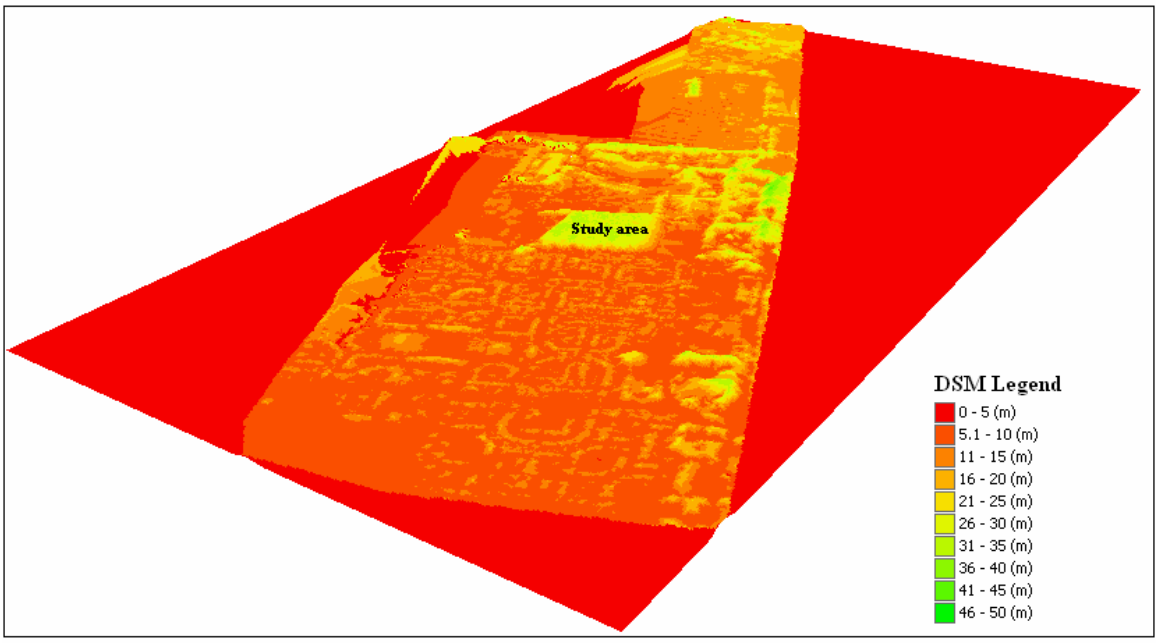

Fig. 9: DSM generated from the NIR image layer with expert DSM generation settings.

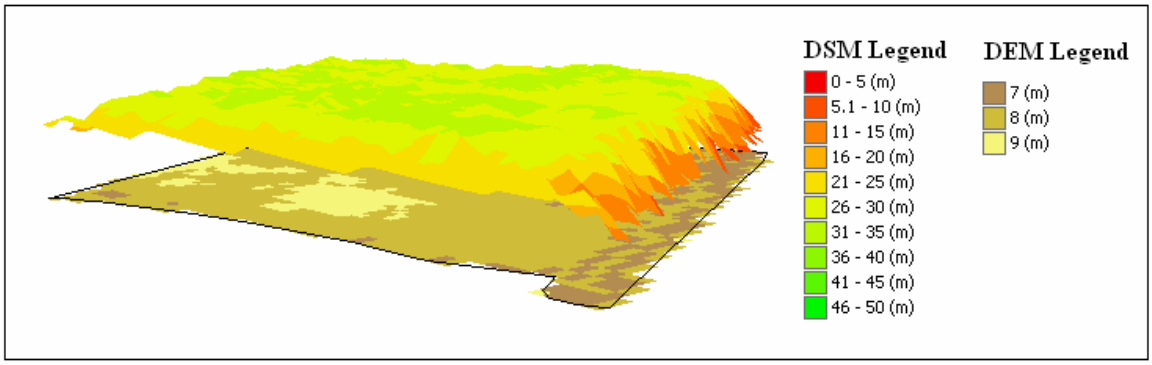

Fig. 10: Study area expert NIR DSM (top) and AHN DEM (bottom).

Table 5: Number of DSM points per image layer.

Image layer		Green	Red	NIR
All DSM	Default	48612	37713	73204
	Expert	43525	39680	81464
Study area DSM	Default	174	25	3051
	Expert	111	12	2728

4.1.4 Layer selection for DSM generation.

According to the best image layer definition (1.2.4) the NIR image layer is the best image layer, with the highest probability to represent accurately terrain feature's heights. The selection of the best image layer is based on the results of table 5. Best image layer selection can have profound implications for the results of AT and subsequently the generation of digital surface and elevation models. Finding a solution, that can indicate the best image layer; can possibly increase the reliability of the DSM/DEM to represent real world features and increase the efficiency of the AT process.

Area based image-matching correlation, functions on grey scale variations (texture) originating from an image's DN values and therefore the image's information content. An indication of the image layer's information content could possibly provide the indication needed for selecting the best image layer to be used in AT. According to Schenk (1999) the Standard Deviation (STDEV) of an image's reflection values can provide an indication for the information content of an image layer. According to this, the red or eventually the green image layer should be used (table 2). This contradicts with the number of DSM points generated by the different image layers (table 5).

The high number of correlated height points, when generating the NIR DSM can be explained by the fact that the STDEV is a measure of the grey scale variance of the entire image (general grey scale variance) and that the image-matching correlation searches for grey level variance within a search window (local grey scale variance). This spatial restriction to a search window size explains why the image matching with the NIR image layer produces almost a double amount of correlated height points than the red or green image layers. This means that the STDEV can only indicate the overall information content, and cannot be used as an indicator for the selection of the best image layer to use in the image-matching process. It is still interesting to note that despite the fact that a great deal of the image shows vegetation, the NIR image layer's STDEV does not show that.

To investigate, wheatear an indication for the best image layer exists in the software, trials made with the automatic tie point generation (TPG) feature. This automatic TPG feature uses the same grey scale image-matching correlation to locate tie points in the stereo images. The trial's results (appendix I) show that the use of TPG does not indicate the best image layer.

4.1.5 Sensitivity analysis.

Table 6 presents a summary of the results from the sensitivity analysis. Detailed information regarding the establishment of the expert DSM generation settings is found in appendix E.

Table 6: Sensitivity analysis results: expert DSM generation settings.

Settings	Default	Expert	Expert	Expert
Image layer used	Red/Green/NIR	Green	Red	NIR
Search window X	21	3	39	9
Search window Y	3	5	19	3
Correlation window X	7	9	5	7
Correlation window Y	7	5	15	7
Coefficient limit	0.80	0.87	0.90	0.89

The results of the sensitivity analysis classification are summarized and presented in table 7. More detailed graphs are found in appendix E.

Table 7: Sensitivity analysis classification summery.

Differences between default and expert DSM extraction settings in %.			
Green layer	Default (%)	Expert (%)	Difference (%)
Excellent	73	78	5
Good	12	9	-3
Fair	8	7	-1
Isolated	5	4	-1
Suspicious	2	2	0
Red layer			0
Excellent	72	76	4
Good	13	10	-3
Fair	8	7	-1
Isolated	5	5	0
Suspicious	2	2	0
NIR layer			0
Excellent	81	84	3
Good	10	7	-3
Fair	5	5	0
Isolated	3	3	0
Suspicious	1	1	0

Investigating the expert DSM generation settings shows that no major improvements, according to the internal validation, can be attained using these settings. However, the validity of the internal validation process is questioned. Investigating the difference between the expert and default settings by the second validation method (second generation AT and orthoDSM generation, which is described later), show that there is a significant difference in the accuracies of these

DSM's (figure 17 and 18). This contradiction tells us about the unreliability of the internal validation process.
The internal validation process, supplied with the used software, give the option to make use of the block's GCP's, checkpoints or tie points. When making use of the GCP's in the internal validation process, one should ask himself if the points used to transform the images into a certain coordinate system and are used as seeds points for DSM extrapolation, can serve as adequate validation data.
When using the tie points, especial attention to the degree of the tie points reliability to display accurately real world feature, should be given. Actually, the only reliable data types to be used are the checkpoints, especially because they are not participating in the AT.
To the amazement of the author, when checking to see if a difference exists in the internal validation classification between using only the GCP's, check point and tie points resulted in the same internal validation classification result. (Appendix I). This, again, gives rise to the adequacy of the internal validation process as a reliable source of validation for DSM's heights. In addition to that, the description of the internal validation classification process does not precisely indicate which other variables, such as the correlation window sizes and the search window sizes, are used.

4.1.6 Orthoimages generation.

The orthorectification process resulted in four orthoimages (two made from by using the default DSM generation settings and two using the expert DSM generation settings) made with the best image layer (i.e. NIR image layer). Despite the fact that no further analysis was carried out on the orthoimages, there are some points that need to be addressed. The overall quality of the orthoimages was not assessed, since this is beyond the scope of this research, but visually a few image deformations were detected. Figure 11 shows an example of image deformation in the NIR orthoimage made with the default DSM and the same location in the NIR orthoimage made with the expert DSM.

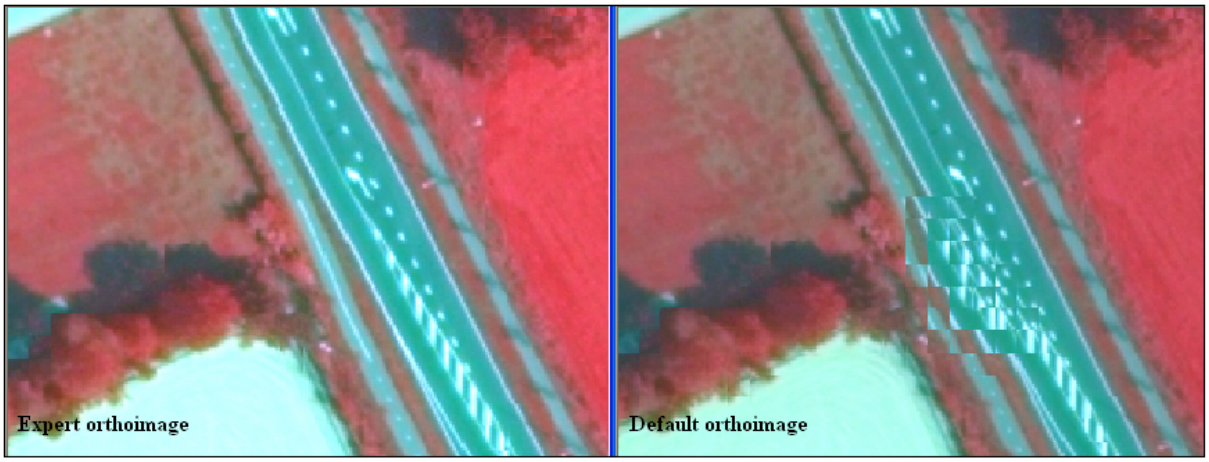

Fig. 11: Example of orthoimage deformation in the orthoimage generated with the default DSM made from the NIR image layer (Right image).

4.2 Validation.

Presented are the results of the AT validation and DSM's validations.

4.2.1 Aerial Triangulation displacement.

The AT displacement statistics (table 9) show that the average displacements in the X and Z axes are within acceptable tolerances (X and Y displacements of 0.3m and Z displacement of 0.9m, based on rule of thumb). The Y displacement, however, is not within those tolerances. When analyzing the Y values of table 8, around 40% of them are equal or bigger than -0.5m, which contribute to the relatively high Y displacement average. The reason for these displacements could be the fact that the LSM runs on the Y-axis of the image.
The X and Y axes average and total displacements are negative, while the Z-axis is positive, this height overestimation originates from the effects of X and Y parallax and relief displacements.

Table 8: AT displacement (m) in the XYZ axes.

Point ID	Description	X	Y	Z
I1-2-1	Tie	-0.3	-1.2	-0.5
I1-3-1	Tie	-0.2	-0.2	-0.6
I1-6-1	Control	0.0	0.0	0.0
I1-6-2	Check	0.0	0.0	0.0
I1-6-3	Tie	-0.1	-0.2	1.3
I1-6-4	Tie	-0.1	-0.4	2.2
I1-6-5	Tie	0.0	-0.5	1.6
I2-1-1	Tie	-0.4	-0.5	0.2
I2-1-2	Tie	-0.4	-0.9	0.6
I2-1-3	Tie	-0.2	-0.4	0.1
I3-1-1	Tie	-0.3	-0.7	1.6
I3-1-2	Tie	-0.1	-0.7	1.4
I3-1-3	Tie	-0.2	-0.8	1.5
I3-1-4	Tie	-0.3	-0.8	1.5
I3-1-5	Tie	-0.3	-0.7	1.5
I3-1-6	Check	0.0	0.0	0.0
I3-2-1	Control	0.0	0.0	0.0
I3-2-2	Tie	-0.3	-0.3	-0.4
I3-2-3	Tie	-0.5	-0.5	-0.8
I3-2-4	Tie	-0.2	-0.6	-0.9
I3-3-1	Tie	-0.4	-0.3	-0.7
I3-3-2	Tie	-0.6	-0.4	-1.7
I3-3-3	Tie	0.2	-0.2	0.7
I3-4-1	Control	0.0	0.0	0.0
I3-4-2	Check	0.0	0.0	0.0
I3-4-3	Tie	-1.0	-0.3	-0.5
I3-4-4	Tie	-0.5	-0.9	0.4
I3-4-5	Tie	-0.4	-0.2	-0.1
I3-4-6	Tie	-0.4	-0.4	0.8
I3-4-7	Tie	0.0	-0.8	-0.4
I3-4-8	Tie	-0.4	-0.5	-1.5
I3-4-9	Tie	-0.5	0.1	0.5
I3-4-10	Tie	-0.1	0.3	1.3
I3-4-11	Tie	-0.2	-0.8	1.4

Table 9: AT displacement statistics (m) in the XYZ axes.

	X	Y	Z
Total	-8.4	-13.8	10.7
Average	-0.3	-0.5	0.4
Maximum	0.2	0.3	2.2
Minimum	-1.0	-1.2	-1.7

4.2.2 DSM - DGPS correlation analysis.

Presented are the results of the second DSM's validation by means of correlation with independent DGPS measurements. The correlation of the DSM', generated with the default DSM generation settings using all image layers, and independent DGPS measurements are presented in figures 12 to 14. Figure 15 presents the correlation between the AHN DSM and independent DGPS measurements. Finally, the DSM's generated with the expert DSM generation settings of all image layers (figures 16 to 18) correlation with independent DGPS measurements are presented.
The linear regression function presents the best fit of the DSM's heights and this line lies, on average, between one meter and two meters above the DGPS 1:1 line. According to the default correlation graphs (figures 12 to 14) the accuracies of the default DSM's generated from all the image layers is low and unacceptable. According to the rule of thumb, an acceptable height estimation lies within ± 0.9 of the real height. From the figures it is clear that the default DSM's height (over)estimations are well beyond this range. The accuracies of the DSM's generated with expert DSM generation settings are slightly better (figures 16 to 18). The best-fit line is closer to the DGPS 1:1 line and the DSM's height points are more concentrated around this line. There is no apparent accuracy differences between the DSM's generated from the different spectral image layers. The range of the heights (over)estimation is similar but, as mentioned before, the number of generated height points is different.
There are, however, significant accuracy differences between the photogrammetric generated DSM's and the AHN DSM, which is an ALS product. Figure 15 clearly, shows that only height overestimation takes place and that no height underestimation takes place. This is due to the nature of the ALS sensor that physically sends and receives a laser pulse from the terrain surface. In the photogrammetric generated DSM's no such physical interaction takes place between the sensor and the surface and that is why height underestimation can take place. The best-fit line confirms the overestimation by reaching beyond the graph extent. Despite that, only 35 AHN DSM points are used to investigate the AHN DSM accuracy the range of height overestimation reflects on the inaccuracy of the 'source' dataset from which the AHN final product is produced.
The possibility to correct the DSM's in a single step exists. This can be done by adding or subtracting the value between the DGPS 1:1 line and the best-fit line to the individual Z values of the DSM's points. The addition or subtraction depend wheatear the DSM points are under or above the DGPS 1:1 line. The result of such a correction is will be a more accurate DSM since the individual DSM points will lay closer to the DGPS 1:1 line, but it will still contain height overestimation and underestimation. The single step correction is possible but with limitations.

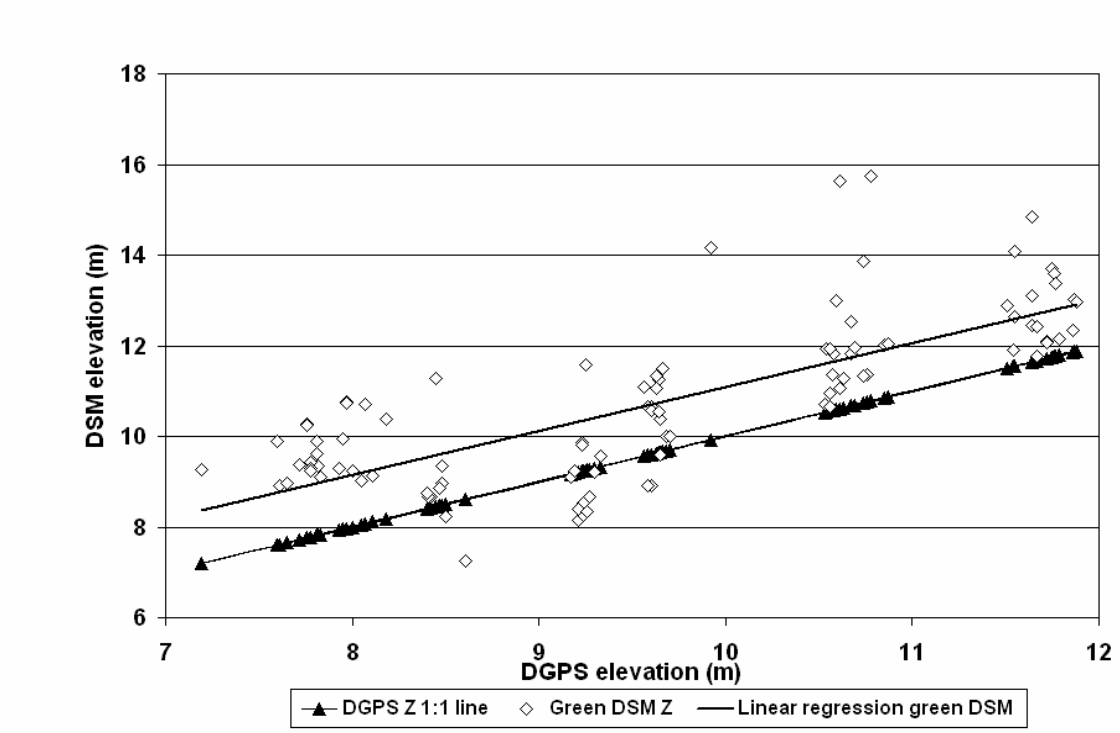

Fig. 12: Result of the correlation between 101 DSM Z values generated with the default DSM generation settings using the green image layer, with independent DGPS measurements.

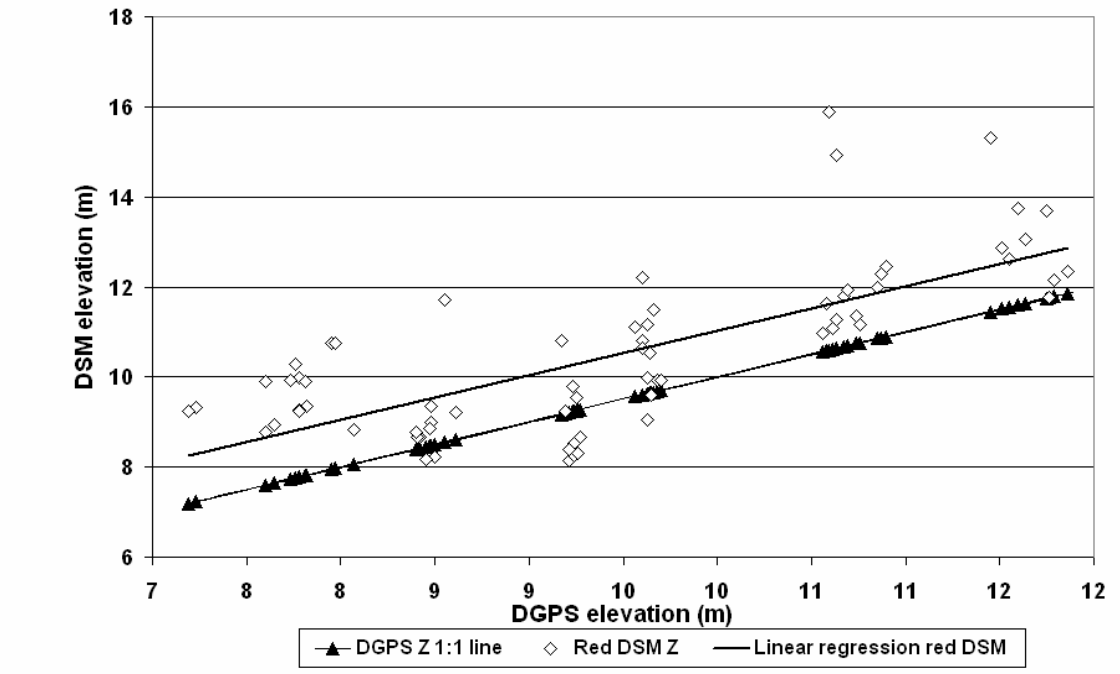

Fig. 13: Result of the correlation between 72 DSM Z values generated with the default DSM generation settings using the red image layer, with independent DGPS measurements.

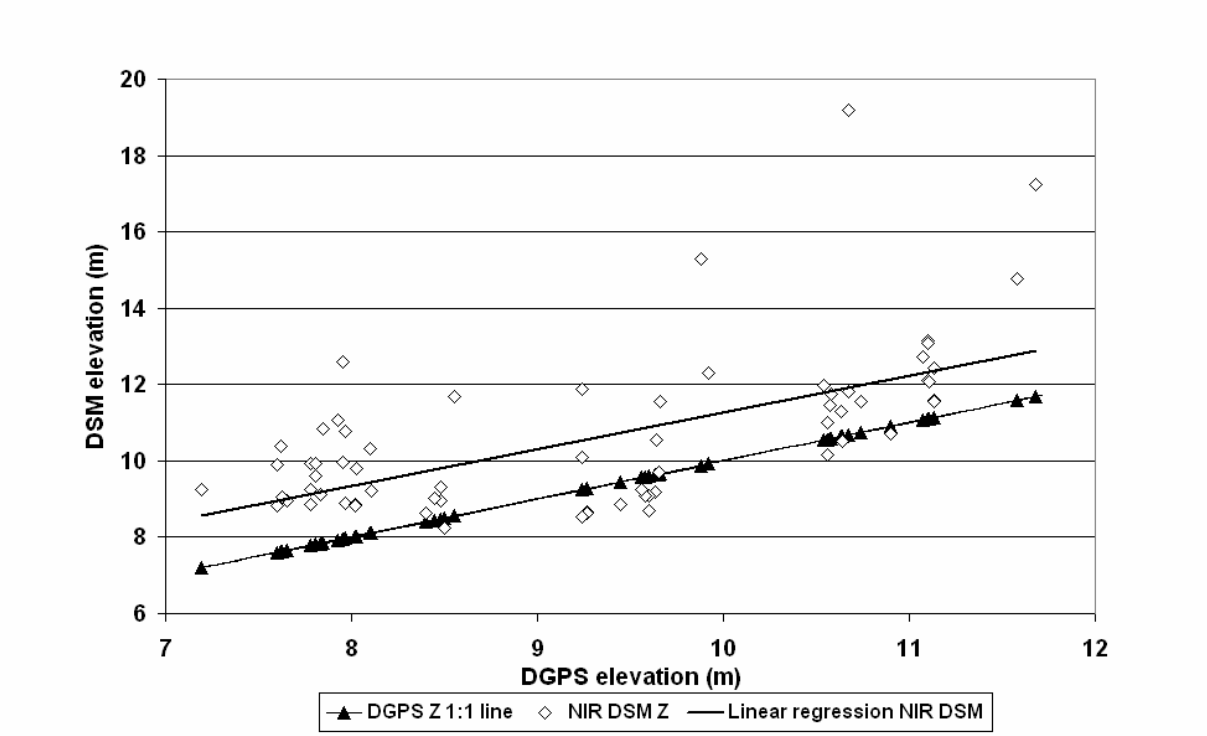

Fig. 14: Result of the correlation between 70 DSM Z values generated with the default DSM generation settings using the NIR image layer, with independent DGPS measurements.

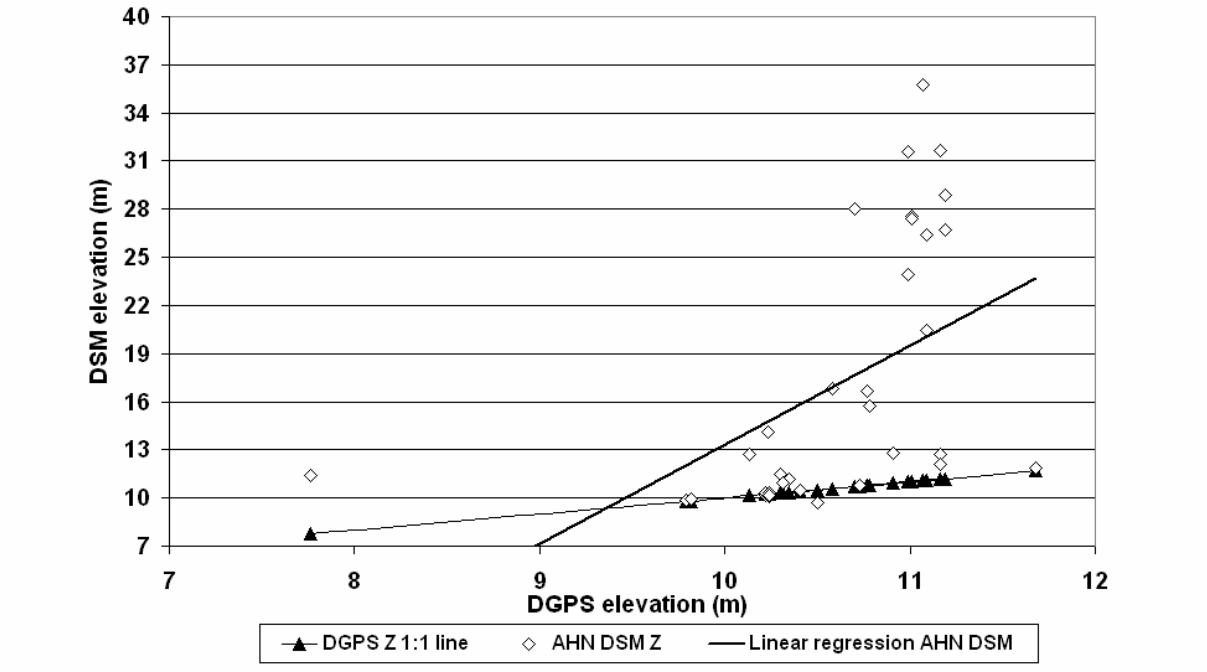

Fig. 15: Result of the correlation between 35 AHN DSM Z values with independent DGPS measurements.

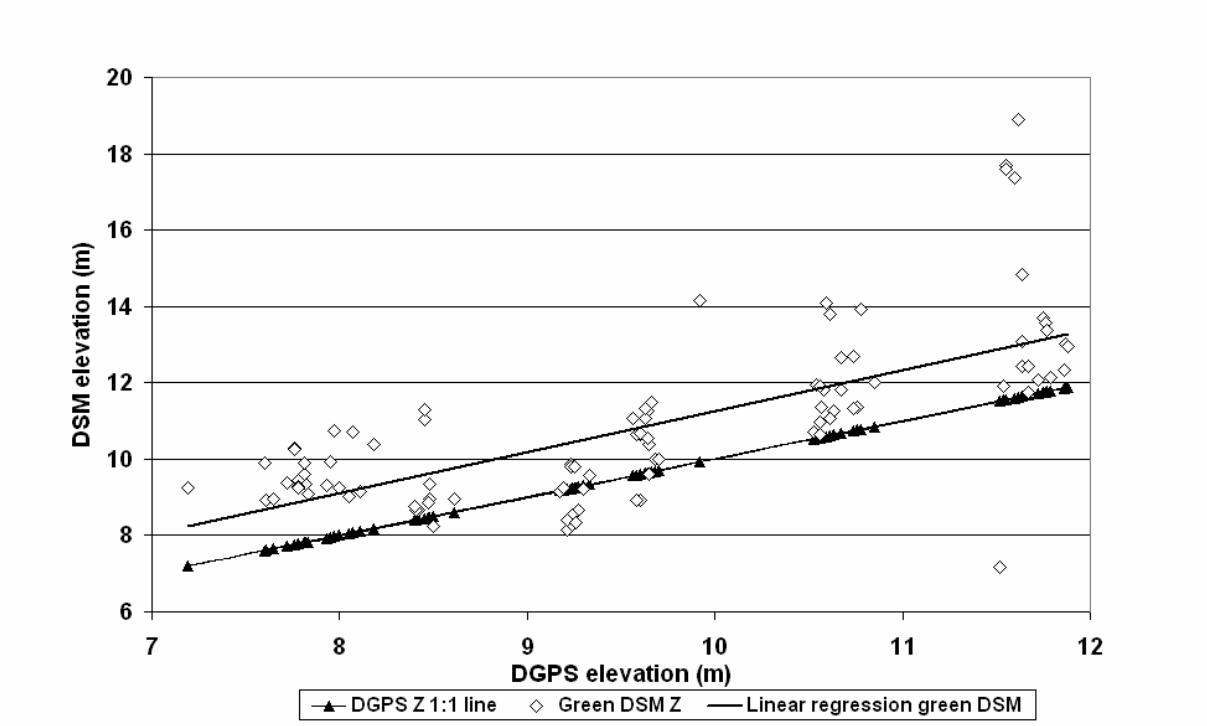

Fig. 16: Result of the correlation between 102 DSM Z values generated with the expert DSM generation settings using the green image layer, with independent DGPS measurements.

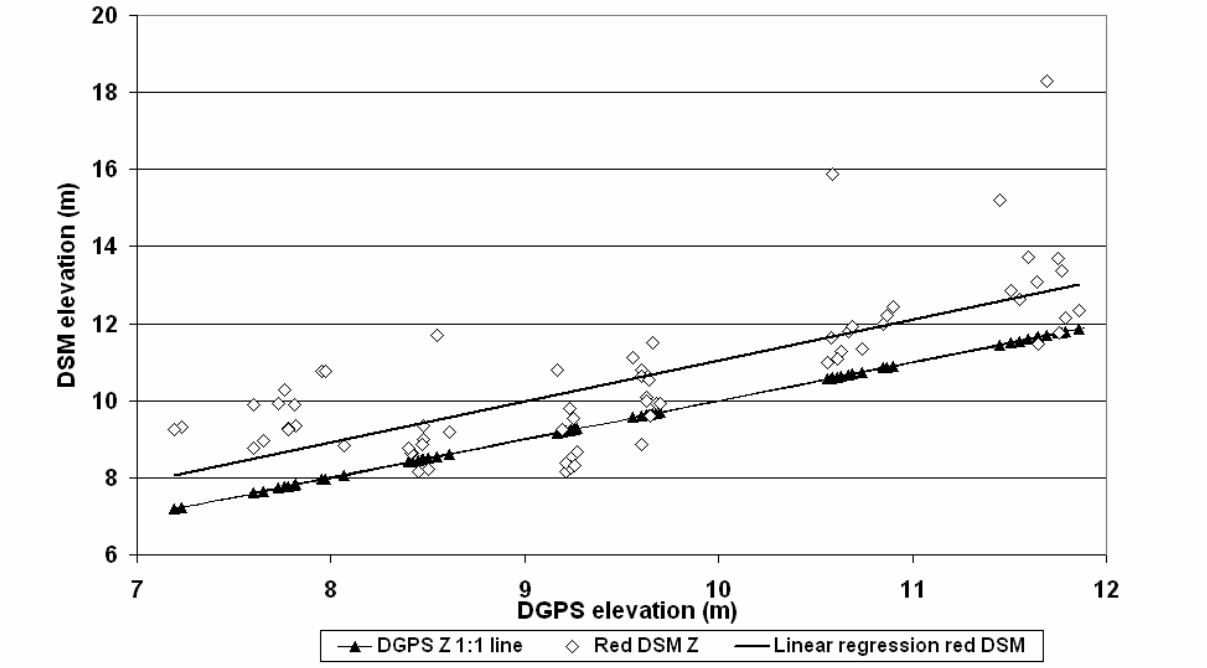

Fig. 17: Result of the correlation between 72 DSM Z values generated with the expert DSM generation settings using the red image layer, with independent DGPS measurements.

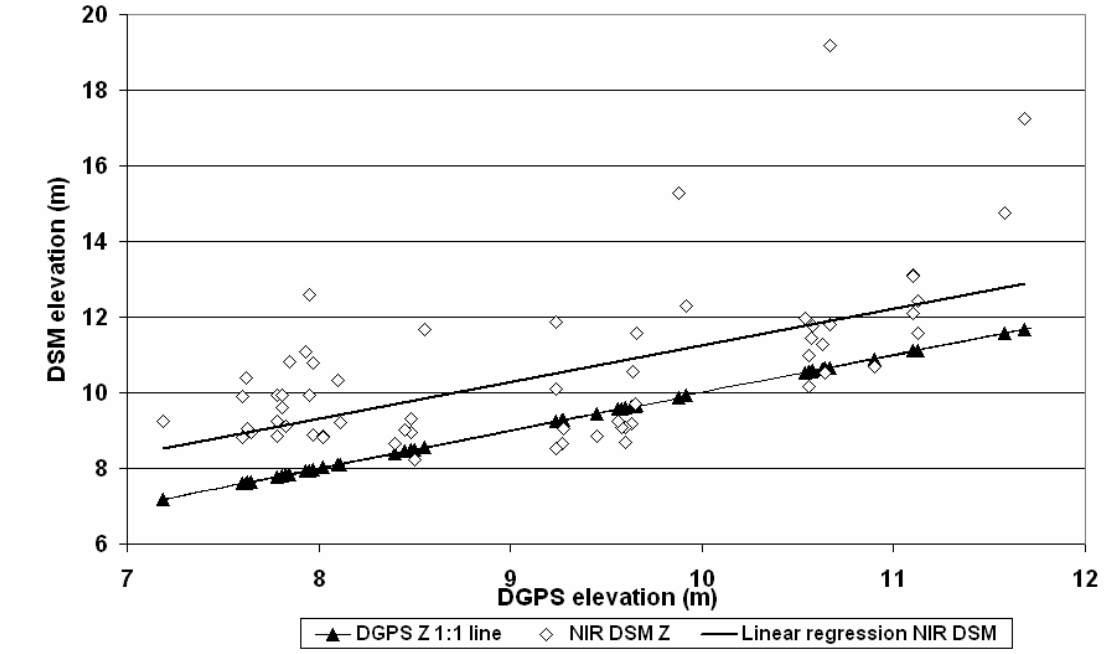

Fig. 18: Result of the correlation between 67 DSM Z values generated with the expert DSM generation settings using the NIR image layer, with independent DGPS measurements.

4.2.3 Spatial representation of DSM height overestimation and underestimation.

Figure 19 is an example of spatial presentation of height differences. The spatial representation can provide an insight to the generation of DSM height point per landscape type (i.e. urban, vegetation, impervious surfaces). Further analysis can be carried out to investigate if a relation exists between landscape type and DSM height overestimation or underestimation. This, however, is beyond the scope of this research.

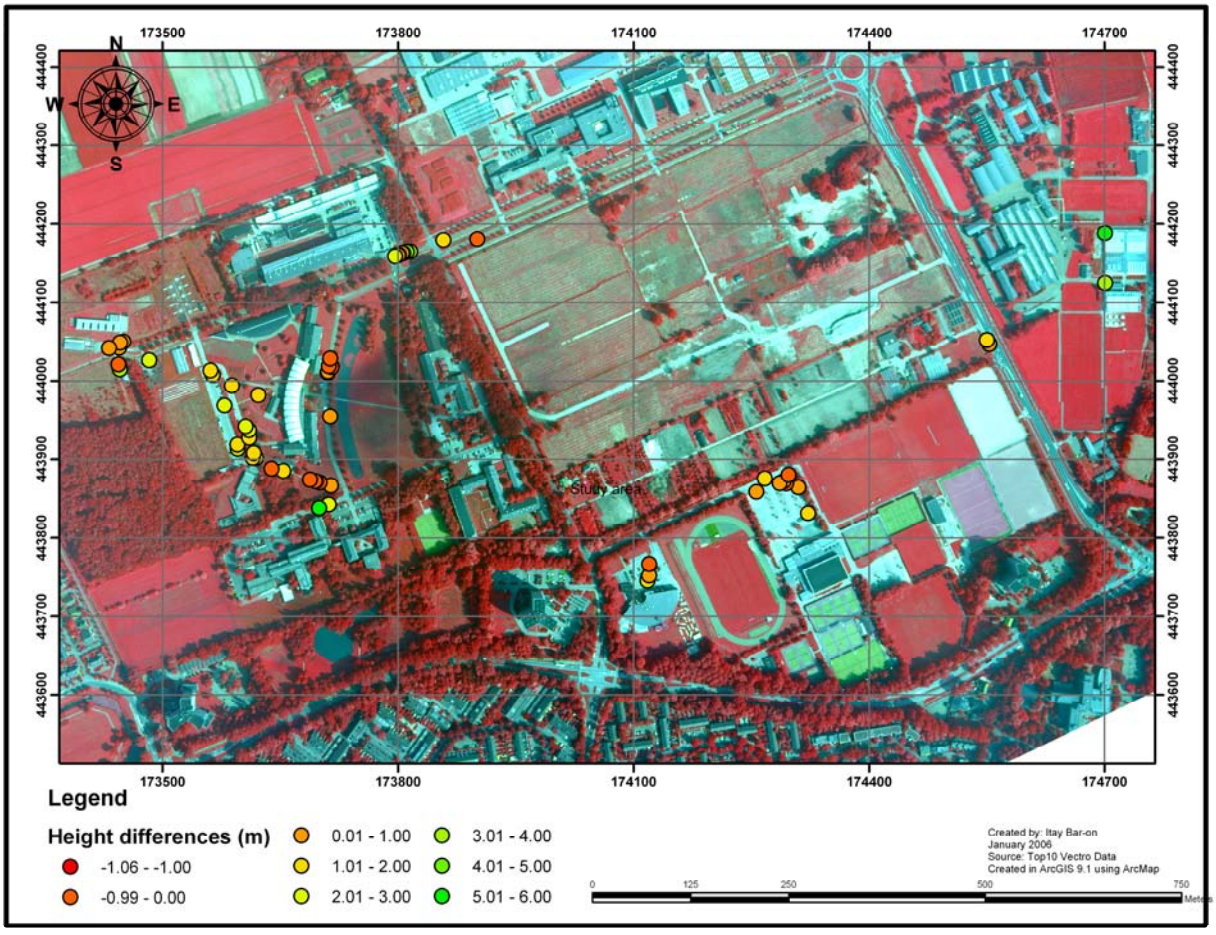

Fig. 19: Spatial presentation of height overestimation and underestimation between the DSM generated using the expert DSM generation settings with the NIR image layer and independent DGPS measurements.

4.2.4 Spatial estimation of DSM generation errors.

The results of the validation method described in 3.2.3 are images with a spatial estimation of DSM generation errors. Figure 20 presents the orthoDSM generated with the NIR image layer using default DSM generation settings and figure 21 shows the same orthoDSM generated with the expert DSM generation settings.
The first apparent difference between figures 20 and 21 is that a difference does exist when using the default and expert DSM generation settings. This contradict with the results of the sensitivity analysis, but one should bare in mind that the sensitivity analysis results are based on the internal validation classification (appendix E) which has already been proven to be unreliable for DSM validation.
There is a substantial difference between the default and expert NIR orthoDSM's. In all of the default NIR orthoDSM extent, unreliable correlation takes place, meaning that the DSM errors are present in almost all of the default DSM extent.
The expert NIR DSM shows overall that correlation is more reliable, especially in the area between the GCP's, where interpolation takes place, a flat orthoDSM results. Toward the orthoDSM edges, where more extrapolation takes place, less reliable correlation results are found. This is also due to the presence of cloud cover in the original images and the urban landscape type.

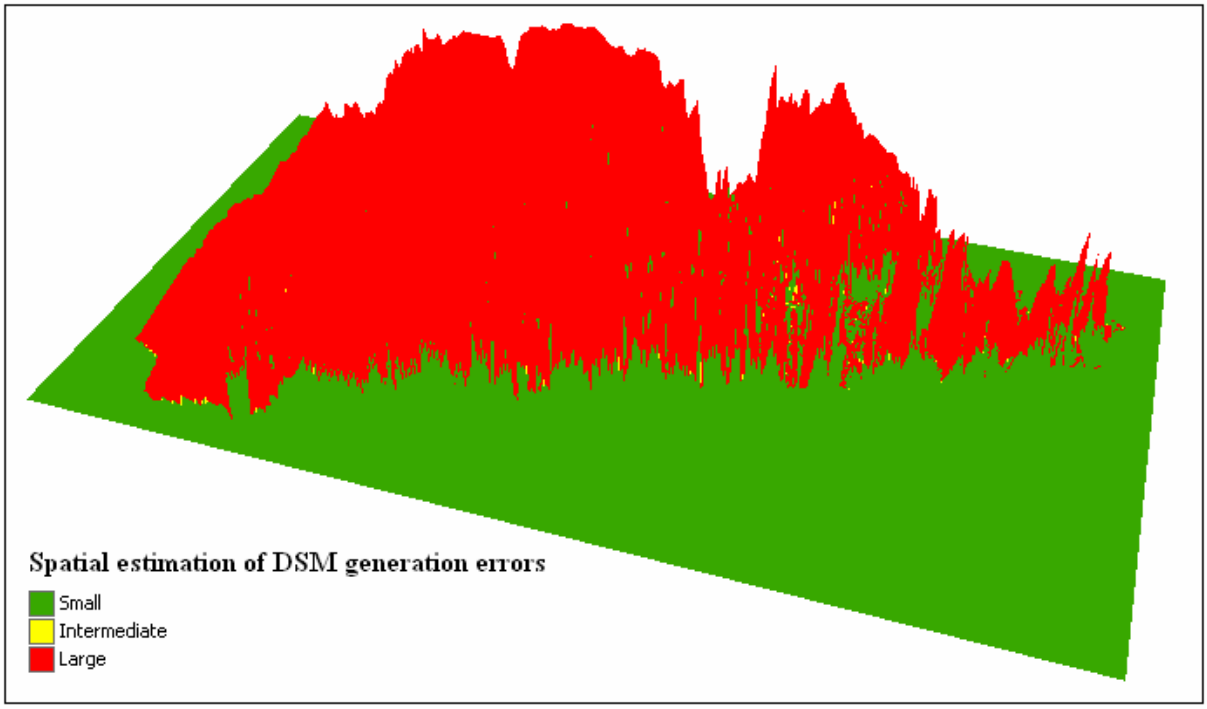

Fig. 20: OrthoDSM generated with default DSM generation settings using the NIR image layer and GCP set B.

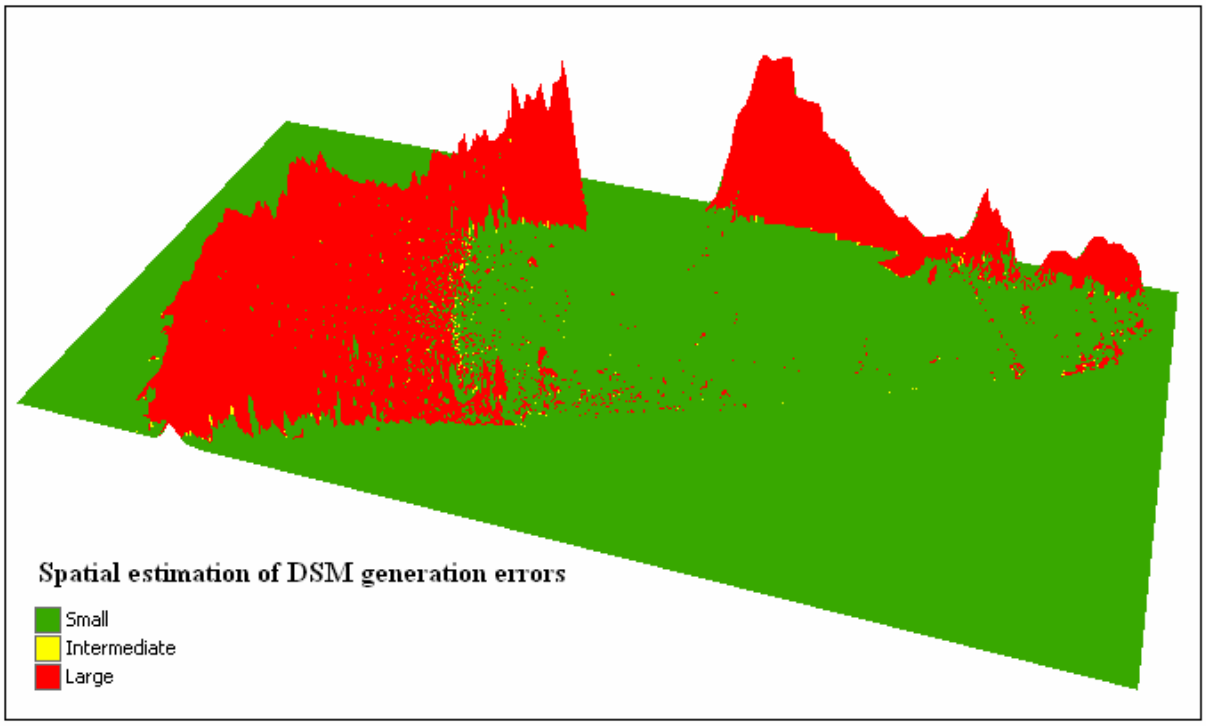

Fig. 21: OrthoDSM generated with expert DSM generation settings using the NIR image layer and GCP set B.

4.2.5 The effect of GCP's distribution on DSM generation.

Presented are the results of the effect of GCP's distribution on the DSM generation. Figure 22 shows the orthoDSM generated with default DSM generation settings using the NIR image layer with GCP set C. Figure 23 shows the effect of GCP's distribution on the DSM generation. The addition of one GCP in the urban area, clearly result in a much flatter orthoDSM.
There are spikes in the heights in both figures; these correlation spikes correspond with areas where water and buildings are present. The combination of these landscapes types results in incorrect correlation because of the high variation in the grey level scale.

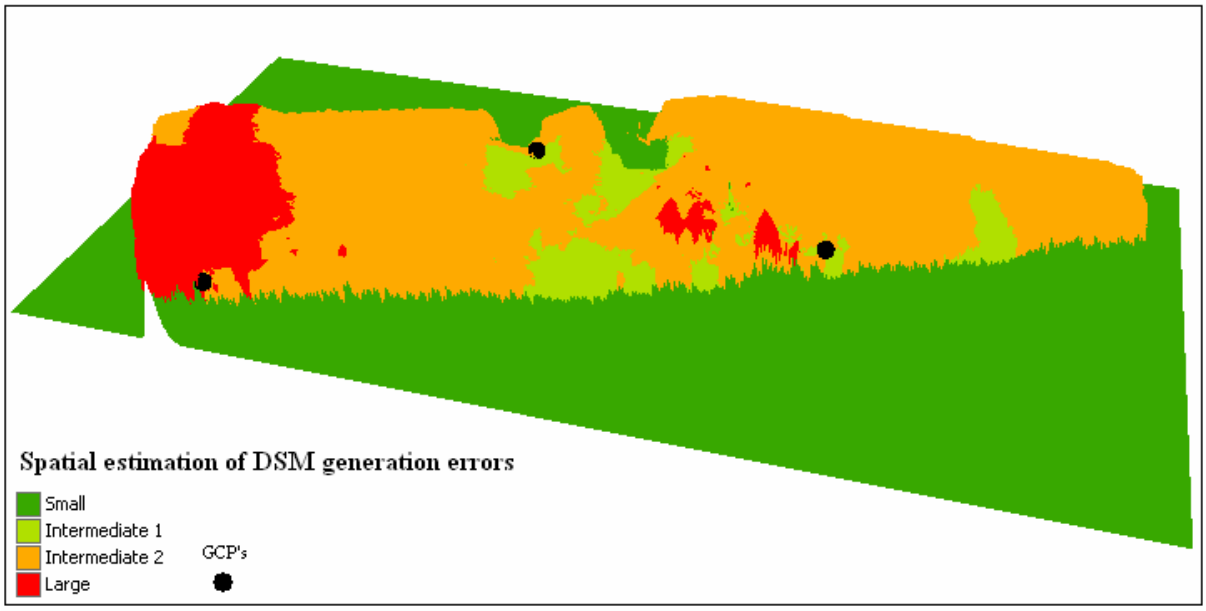

Fig. 22: Default NIR orthoDSM with GCP set C.

Fig. 23: Default NIR orthoDSM with GCP set D.

4.3 Application.

Presented are the results of the estimation of forest volume.

4.3.1 Forest volume estimation via conventional forestry measurements.

The study area can be characterised as a former production forest ("Rabattenbos") presumably abandoned for the last 50 years.
The results of the sampling done in the study area are the specie composition, which helps to characterize the study area. The dominant tree species are oak (Quercus robur), Common Alder (Alnus glutinosa) and European white birch (Betula Pendula). Table 10 presents the total average tree volume of the study area estimated by conventional forestry measurements. Table 11 shows the estimated tree volume according to tree specie and per plot. Table 12 presents the estimated tree volume according to tree specie and per square meter. All of these results are derived from the tree data in appendix G.

Table 10: Summery of volume estimation via forestry measurements.

	Total volume (m^3/plot)	Plot radius (m^2)	Surface (m^2)	m^3/m^2	m^3/Ha	Average m^3/Ha
Plot 1	11.2	10	314*	0.025	250.0	
Plot 2	11.6	10	314*	0.037	370.0	
Plot 3	13.8	12	452*	0.044	440.0	
Study area			35723**			353.3

* Surface = Phi * plot radius²
** Study area surface from modified extent.

Table 11: Summary of volume estimation per specie per plot.

Plot number	QR (m^3/plot)	BP (m^3/plot)	Alnus (m^3/plot)	Total (m^3/plot)
Plot 1	5.40	4.68	1.13	11.20
Plot 2	9.36	1.43	0.81	11.60
Plot 3	12.95	0.88	0.00	13.83

QR = Quercus Robur (Oak).
BP = Betula Pendula (Birch).
Alnus = Alnus glutinosa (Alder).

Table 12: Summary of volume estimation per specie per square meter.

Plot number	QR (m^3/m^2)	BP (m^3/m^2)	Alnus (m^3/m^2)
Plot 1	0.012	0.010	0.003
Plot 2	0.030	0.005	0.003
Plot 3	0.041	0.003	0.000
All plots average	0.028	0.006	0.002

QR = Quercus Robur (Oak).
BP = Betula Pendula (Birch).
Alnus = Alnus glutinosa (Alder).

The results of the volume estimation show that the study area's tree volume is relatively high. This is due to the lack of management in the study area and the high tree density. Oak (Quercus robur) is the dominant tree specie with the highest volume in all three sample plots and the highest average volume per square meter.

4.3.2 Forest volume estimation via DSM and image segmentation.

Figure 24 shows the segmented image used in the individual tree number estimation. According to this estimation, there are 390 individual trees in the study area.
More DSM and image segmentation trials are in appendix H.

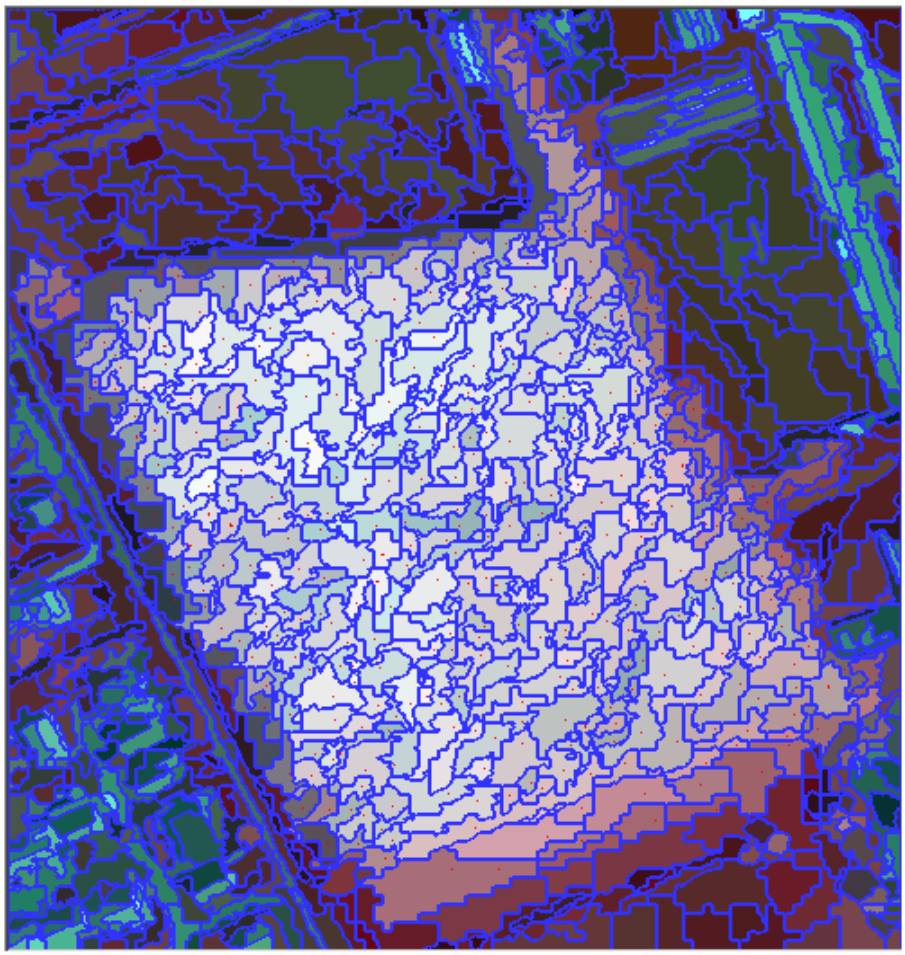

Fig. 24: Segmented image used for individual tree numbers estimation. Every dot represents one tree canopy estimated.

Table 13: Estimated tree number per specie, according to specie dominance, in the study area.

Specie	QR	BP	Alnus	Total
Tree number	245	105	40	390

QR = Quercus Robur (Oak).
BP = Betula Pendula (Birch).
Alnus = Alnus glutinosa (Alder).

4.3.3 Forest volume comparison.

According to the estimated number of individual trees (table 13) and the average specie volume presented in table 12, the resulting tree volume estimated via DSM and image segmentation of the study area are presented in table 14.

Table 14: Individual tree volume estimation via DSM and image segmentation and comparison with tree volume derived from forestry measurements.

Specie	QR	BP	Alnus	Total	
Average specie volume (m^3/study area)	6.78	0.62	0.07	7.46	
Volume (m^3/Ha) via DSM/image segmentation					2.13
Volume (m^3/Ha) via forestry measurements					353.30

QR = Quercus Robur (Oak).
BP = Betula Pendula (Birch).
Alnus = Alnus glutinosa (Alder).

The results of the segmentation trials and volume comparison show that the gap between Remote Sensing (RS) measurements and conventional forestry measurements is still too large to be able to compare directly RS and forestry measurements. The estimated tree volume via DSM/image segmentation (2.13 m^3/Ha) is very low in comparison with the tree volume derived from the forestry measurements (353.30 m^3/Ha). The number of estimated individual trees, via DSM and image segmentation, is too inaccurate to provide correct and reliable information about individual trees physical characteristics. The accurate estimation of physical characteristics such as tree volume, height and health from the generated DSM and images cannot take place. In addition, the fact that the volume estimation relays on field data and not data extracted directly from the images, gives an indication to the gap size between RS measurements and conventional forestry measurements.

5 Conclusions and recommendations.

The research conclusions and recommendations are presented according to the research report structure. First the conclusions and the recommendations concerning the research products are presented, followed by the conclusions and recommendations of the research validation methods and finally the conclusions and recommendations regarding the research application.

5.1 Research products.

5.1.1 Conclusions and recommendations concerning research products.

- The application of the area based image-matching correlation works well in creating stereo images from overlapping high-resolution images.
- Acceptable aerial triangulation results, with high-resolution aerial imagery, are achieved.
- The generated DSM's tend to overestimate terrain heights.
- GCP's distribution affects the DSM's generation and the reliability to estimate accurately terrain heights.
- Expert DSM generation settings do result in a flatter orthoDSM than default settings.

The main recommendations regarding the research products are to investigate the image geometric and radiometric qualities of the original digital aerial images. These image properties such as signal structure and signal-to-noise ratio have effects on the image matching, AT and consequently DSM generation. An investigation to asses the image radiometric and geometric qualities can provide insight to the selection of the best image layer.
Before AT takes place, the measurement of GCP's is done. As demonstrated the distribution of the GCP's have a significant effect on the DSM accuracies, therefore it is recommended that optimal GCP's distribution should be researched and established. It is also recommended to increase the block size from one model to three models to see if the potential of the methodology can be applied to bigger block sizes. The spatial estimation of DSM generation errors should be researched with other photogrammetric software packets to find out if the research methodology is applicable with them.
The possibility of a single step correction to the DSM's is demonstrated in the research. Further investigation to carry out the correction should take place.
Since orthoimages and their generation play an important role in the methodology. It is recommended that future research applying the same methodology should develop a way to assess the orthoimages generation and the geometric quality of the orthoimages generated.

5.2 Validation methods.

5.2.1 Conclusions and recommendations concerning the validation methods.

- The internal validation process (i.e. "DTM Point Status Image") is unreliable and should not be used for DSM validation, but can be used to establish DSM generation settings.
- The accuracy of the AHN DSM, an ALS product and the 'source' dataset for the production of the final AHN DEM product, is low in comparison with the photogrammetric derived DSM's.
- The results show that there is a potential in the spatial estimation of DSM generation errors.

The main recommendation of the validation methods is that the internal validation process (i.e. "DTM Point Status Image") should not be used to asses DSM's accuracies. The lack of detailed information concerning the processes involved in the internal validation procedure and the amazing result when using different block points for the internal validation (table 17) demonstrate the lack of reliability of this internal validation procedure. However, the definition of (expert) DSM generation settings can be done by using of the internal validation process. It is recommended to investigate the definition and application of DSM generation settings according to land use type.
It is also recommended to increase the number of independent DGPS control points used in the validation of the DSM's since this will allow for a better selection and a higher number of points to correlate with the DSM'S points.
More research should take place toward the development of an independent spatial DSM error estimation tool based on orthoimages properties and through orthoimages triangulation.

5.3 Application.

5.3.1 Conclusions and recommendations concerning the research application.

- Accurate forest volume estimation cannot be made directly from the generated DSM's and UltraCam images.
- The accurate estimation of individual tree numbers through DSM and image segmentation is not possible.

The research application demonstrated that, at this point, deriving forest characteristics, directly from the RS measurements is not possible. Therefore, more research should be done to investigate DSM, DSM derivatives (i.e. slope and curvature) and image segmentations for accurate and direct forest characteristics estimation from RS imagery. This can lead to a narrowing of the gap between RS measurements and conventional forestry measurements and to, possibly, directly deriving forest information from RS imagery.

6 Literature.

(Anon), 1992. Kyoto protocol to the United Nations framework convention on climate change, United Nations, Kyoto.

Ackermann, F., 1984. Digital image correlation: performance and potential application in photogrammetry. The Photogrammetric Record, 11(64): 429-239.

Ackermann, F. and Krzystek, P., 1991. Match-T: Automatic Mensuration of Digital Elevation Models. Sistemas Fotogrametricos Analiticos Digitales: 67-74.

Andersen, H.-E. et al., 2005. Estimating forest canopy fuel parameters using LIDAR data. Remote Sensing of Environment, 94(4): 441-449.

Anttila, P., 2002. Nonparametric estimation of stand volume using spectral and spatial features of aerial photographs and old inventory data. Canadian Journal of Forest Research, 32: 1849-1857.

ASP, 1980. Manual of Photogrammetry. Manual of Photogrammetry, 4. American Society of Photogrammetry

Baltsavias, E.P., 1999. A comparison between photogrammetry and laser scanning. ISPRS Journal of Photogrammetry and Remote Sensing, 54(2-3): 83-94.

Baltsavias, E.P., 2004. Object extraction and revision by image analysis using existing geodata and knowledge: current status and steps towards operational systems. ISPRS Journal of Photogrammetry and Remote Sensing, 58(3-4): 129-151.

Blackburn, G.A., 2002. Remote sensing of forest pigments using airborne imaging spectrometer and LIDAR imagery. Remote Sensing of Environment, 82(2-3): 311-321.

Bortolot, Z.J. and Wynne, R.H., 2005. Estimating forest biomass using small footprint LiDAR data: An individual tree-based approach that incorporates training data. ISPRS Journal of Photogrammetry and Remote Sensing, 59(6): 342-360.

Brown, J.R. and Carter, J., 1998. Spatial and temporal patterns of exotic shrub invasion in an Australian tropical grassland. Landscape Ecology, 13: pp. 93–102.

Burtch, R., 2000. Analytical photogrammetry lecture notes, The Center for Photogrammetric Training.

Caylor, J., 2000. Aerial photography in the next decade. Journal of Forestry(98): 17-19.

Couteron, P., 2002. Quantifying change in patterned semi-arid vegetation by Fourier analysis of digitized aerial photographs. International Journal of Remote Sensing, 23(17): pp. 3407-3425(19).

Cramer, M. and Stallmann, D., 2001. On the use of GSP/Inetrial exterior orientation parameters in airborne photogrammetry, ISPRS workshop 'High Resolution Mapping from Space', Hannover.

Culvenor, D.S., 2002. TIDA: an algorithm for the delineation of tree crowns in high spatial resolution remotely sensed imagery. Computers & Geosciences, 28(1): 33-44.

Ebadi, H., 1997. A compreansive study on GPS assisted aerial triangulation, University of Calgary, Calgary, 209 pp.

Elmore, A.J. et al., 2000. Quantifying Vegetation Change in Semiarid Environments: Precision and Accuracy of Spectral Mixture Analysis and the Normalized Difference Vegetation Index. Remote Sensing of Environment, 73(1): 87-102.
Filin, S., 2004. Surface classification from airborne laser scanning data. Computers & Geosciences, 30(9-10): 1033-1041.
Forstner, W., 1995. Matching strategies for point Transfer, Photogrammetric Week, Stutgart, Germany, pp. 173-183.
Forstner, W., 1982. On the geometric precision of digital correlation. International Archives for Photogrammetry and Remote Sensing, 24(3): 176-189.
Forstner, W., 1984. Quality assessment of object location and point transfer using digital image correlation techniques. International Archives for Photogrammetry and Remote Sensing, 25(3): 197-220.
Gillis, M.D. and Leckie, D.G., 1993. Forest inventory mapping procedures across Canada. Petawawa National Forestry Institute, Chalk River, 79 pp.
Goslee, S.C. et al., 2003. High-resolution images reveal rate and pattern of shrub encroachment over six decades in New Mexico, U.S.A. Journal of Arid Environments, 54(4): 755-767.
Gougeon, F., 1999. Automatic individual tree crown delineation using a valley-following algorithm and a rule-based system, In Proceedings of the International Forum on Automated Interpretation of High Spatial Resolution Digital for Forestry. Natural Resources Canada, Canadian Forest Service, Pacific Forestry Centre, Victoria BC, pp. 11-23.
Greenberg, J.A. et al., 2005. Shadow allometry: Estimating tree structural parameters using hyperspatial image analysis. Remote Sensing of Environment, 97(1): 15-25.
Grun, A., 1985. Adaptive least-squares correlation: a powerful image matching technique. South Africa Journal of Photogrammetry, Remote Sensing and Cartography, 14(3): 175-187.
Grun, A. and Baltsavias, E., 1987. High-presicion image matching for digital terrain model generation. Photogrammetria, 42: 97-112.
Hall, R.J. and Fent, L., 1996. Influence of aerial film spectral sensitivity and texture on interpreting images of forest species composition. Canadian journal of remote sensing, 22: 350-359.
Heipke, C., 1996. Overview of image matching techniques, OEEPE - Workshop on the Application of Digital Photogrammetric Workstations, pp. 173-189.
Heipke, C., 1997. Automation of Interior, Relative and Absolute Orientation. JPRS Journal of Photogrammetry and remote Sensing, 52(1): 1-19.
Helava, U., 1978. Digital correlation in photogrammetric terrain elevation extraction. Photogrammetria, 34: 19-41.
Hobrough, G., 1959. Automatic stereoplotting. Photogrammetric Engineering and Remote Sensing, 25(5): 763-769.
Hobrough, G., 1978. Digital on-line correlation. Bildmessung und Luftbildwesen, 46(3): 79-86.
Holmgren, P., 1998. Satellite remote sensing for forestry planning - A review. Scandinavian Journal of Forest Research, 13(1): 90 -110.
Hudak, A.T. et al., 2002. Integration of lidar and Landsat ETM+ data for estimating and mapping forest canopy height. Remote Sensing of Environment, 82(2-3): 397-416.

Hudak, A.T. and Wessman, C.A., 2001. Textural analysis of high resolution imagery to quantify bush encroachment in Madikwe Game Reserve, South Africa, 1955-1996. International Journal of Remote Sensing, 22(14): 2731 - 2740.
Hwang, P.A. et al., 2000. Airborne Scanning Lidar Measurement of Ocean Waves. Remote Sensing of Environment, 73(2): 236-246.
Hyvonen, P. et al., 2005. Segment-level stand inventory for forest management. Scandinavian Journal of Forest Research, 20(1): 75-84.
Ip, A.W.L., 2005. Analysis of Integrated Sensor Orientation for Aerial Mapping, University of Calgary, Calgary, 202 pp.
Konecny, G., 1994. New Trends in Technology, and their Application: Photogrammetry and Remote Sensing-From Analog to Digital, Thirteenth United Nations Regional Cartographic Conference for Asia and the Pacific, Beijing, China.
Korpela, I., 2004. Individual tree measurement by means of digital aerial photogrammetry. Silva Fennica(3): 93 p.
Kraus, K. and Pfeifer, N., 1998. Determination of terrain models in wooded areas with airborne laser scanner data. ISPRS Journal of Photogrammetry and Remote Sensing, 53(4): 193-203.
Kreiling, W., 1976. Automatische Herstellung von Hohenmodellen und Orthophotos aus Stereobildern durch digitale Korrelation., Universitat Karlsruhe.
Laliberte, A.S. et al., 2004. Object-oriented image analysis for mapping shrub encroachment from 1937 to 2003 in southern New Mexico. Remote Sensing of Environment, 93(1-2): 198-210.
Leckie, D.G. et al., 2003. Stand delineation and composition estimation using semi-automated individual tree crown analysis. Remote Sensing of Environment, 85(3): 355-369.
Lefsky, M.A. et al., 1999. Surface Lidar Remote Sensing of Basal Area and Biomass in Deciduous Forests of Eastern Maryland, USA. Remote Sensing of Environment, 67(1): 83-98.
Maltamo, M. et al., 2004. Estimation of timber volume and stem density based on scanning laser altimetry and expected tree size distribution functions. Remote Sensing of Environment, 90(3): 319-330.
Mostafa, M.M.R. and Hutton, J., 2005. 10 years of Direct Georeferencing For Airborne Photogrammetry. 11: 33-41.
Mucher, 2003. Monitoren van kleine landschapselementen met IKONOS satellietbeelden. Alterra report 831, CGI report 03-008, Alterra, Wageningen.
Nilsson, M., 1996. Estimation of tree heights and stand volume using an airborne lidar system. Remote Sensing of Environment, 56(1): 1-7.
Pekkarinen, A., 2002. Image segment-based spectral features in the estimation of timber volume. Remote Sensing of Environment, 82(2-3): 349-359.
Priestnall, G., Jaafara, J., Duncanb, A., 2000. Extracting urban features from LiDAR digital
surface models. Computers, Environment and Urban Systems, 24: 65-78.
Rango, A. et al., 2000. Morphological Characteristics of Shrub Coppice Dunes in Desert Grasslands of Southern New Mexico derived from Scanning LIDAR. Remote Sensing of Environment, 74(1): 26-44.
Rosenholm, D., 1987. Least - squares matching method:some experimental results. The Photogrammetric Record, 12(70): 493-512.

Schenk, T., 1996. Automatic Generation Of DEM's: Digital Photogrammetry.
Schenk, T., 1997. Towards automatic aerial triangulation. ISPRS Journal of Photogrammetry and Remote Sensing, 52(3): 110-121.
Schenk, T., 1999. Digital Photogrammetry, 1. Terra Science, 428 pp.
Schiewe, J., 2003. Integration of multi-sensor data for landscape modeling using a region-based approach. ISPRS Journal of Photogrammetry and Remote Sensing, 57(5-6): 371-379.
Schmidt, F., 2001. Generation and analysis of digital terrain models for agricultural application. In: G. Grenier and S. Blackmore (Editors), 3rd European Conference on Precision Agriculture, Montpellier.
Suarez, J.C. et al., 2005. Use of airborne LiDAR and aerial photography in the estimation of individual tree heights in forestry. Computers & Geosciences, 31(2): 253-262.
Thurgood, J. and Mikhail, E., 1982. Photogrammetric analysis of digital images. International Archives for Photogrammetry and Remote Sensing, 24(3): 576-590.
Trinder, e.a., 2002. Aspects of digital elevation models determination, Symposium on Geospatial Theory, Processing and Applications., Ottawa.
Tuominen, S. et al., 2003. Combining remote sensing, data from earlier inventories, and geostatistical interpolation in multisource forest inventory. Canadian Journal of Forest Research, 33: 624-634.
Vosselman, G. et al., 2005. The utilisation of airborne laser scanning for mapping. International Journal of Applied Earth Observation and Geoinformation, 6(3-4): 177-186.
Wang, J. et al., 2003. GPS/INS Integration: A Performance Sensitivity Analysis. Wuhan University Journal of Nature 8(2B): 508-516.
Wulder, M. et al., 2000. Local Maximum Filtering for the Extraction of Tree Locations and Basal Area from High Spatial Resolution Imagery. Remote Sensing of Environment, 73(1): 103-114.
Wulder, M.A. and Franklin, S.E., 2003. Remote sensing of forest environments : concepts and case studies. Kluwer Academic Publishers, Boston [etc.], 519 pp.
Yastikli, N. and Jacobsen, K., 2005. Influence of system calibration on direct sensor orientation. Photogrammetric Engineering and Remote Sensing, 71(5): 629-633.
Zimble, D.A. et al., 2003. Characterizing vertical forest structure using small-footprint airborne LiDAR. Remote Sensing of Environment, 87(2-3): 171-182.

Appendixes.

The appendixes contain more detailed information regarding the research materials, measurements and results.

A. GCP's.

Table 15 present the measured locations of the GCP's sets in RD coordinates (X and Y) and meters (Z).

Table 15: GCP's sets locations.

Set A			
Description	X	Y	Z
I1-6-1	173978.14	445070.58	11.15
I3-2-1	172950.34	443262.79	7.11
I3-4-1	172718.78	444158.93	7.58
Set B			
I1-2-1	174162.14	443800.22	10.69
I2-1-1	173430.50	444042.12	8.43
I3-1-3	174515.28	444141.56	11.19
I3-1-6	174559.84	444054.60	11.39
I3-2-4	172960.27	443261.44	7.08
Set C			
I1-2-1	174162.14	443800.22	10.69
I2-1-3	173415.89	444032.23	8.28
I3-2-1	172950.34	443262.79	7.11
I3-4-1	172718.78	444158.93	7.58
Set D			
I1-2-1	174162.14	443800.22	10.69
I2-1-3	173415.89	444032.23	8.28
I3-2-1	172950.34	443262.79	7.11

B. AT checkpoints.

Table 16 present the AT checkpoint locations in RD coordinates (X and Y) and meters (Z). These checkpoints are used to evaluate the AT result via the AT statistical overview and are used as tie points in the AT displacement analysis.

Table 16: Checkpoints locations.

Point ID	Description	X	Y	Z
1	I1-2-1	174162.14	443800.22	10.69
2	I1-3-1	173298.33	443466.41	7.92
4	I1-6-2	173975.57	445065.69	11.08
6	I1-6-4	173981.12	445076.14	11.23
8	I2-1-1	173430.50	444042.12	8.43
9	I2-1-2	173430.83	444046.75	8.36
10	I2-1-3	173415.89	444032.23	8.28
26	I3-1-1	174512.60	444144.00	11.19
27	I3-1-2	174513.73	444144.61	11.15
28	I3-1-3	174515.28	444141.56	11.19
29	I3-1-4	174557.23	444056.81	11.40
30	I3-1-5	174558.41	444057.36	11.37
31	I3-1-6	174559.84	444054.60	11.39
34	I3-2-3	172959.54	443264.75	7.16
35	I3-2-4	172960.27	443261.44	7.08
36	I3-3-1	172759.69	443214.24	7.45
37	I3-3-2	172757.79	443209.93	7.42
38	I3-3-3	172755.13	443216.18	7.38
40	I3-4-2	172728.59	444170.57	7.69
41	I3-4-3	172721.48	444167.31	7.63
42	I3-4-4	172728.45	444161.61	7.65
43	I3-4-5	172729.71	444163.70	7.67
44	I3-4-6	172726.87	444174.75	7.70
45	I3-4-7	172717.47	444178.84	7.67
46	I3-4-8	172721.03	444172.73	7.62
47	I3-4-9	172715.12	444168.80	7.61
48	I3-4-10	172712.76	444160.97	7.61
49	I3-4-11	172711.63	444175.97	7.65

C. Independent DGPS control points.

The location of all of the independent DGPS control points not involved in the AT and used in the DSM's – DGPS correlation analysis are presented in figure 25.

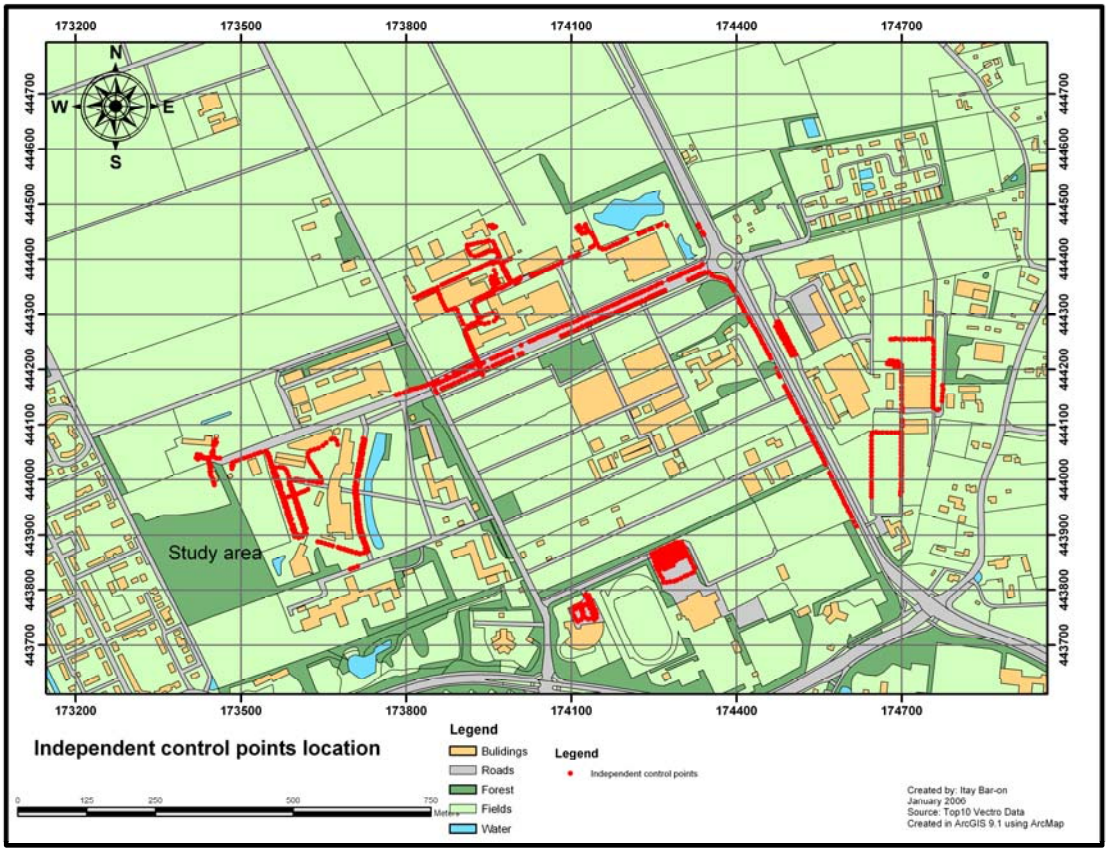

Fig. 25: Independent control point locations, measured with DGPS bike.

D. AT reports.

The detailed reports of the AT preformed with the first two GCP's sets are presented.

First generation AT report for all image layers.

```
        The Triangulation Report With OrthoBASE

        The output image x, y units:     pixels
        The output angle unit:         gons
        The output ground X, Y, Z units: meters

             The Input Image Coordinates
                    image ID = 1
Point ID              x              y
      1         4715.666       1756.578
      2         8414.875       2027.625
      3         3209.440       6763.393
      4         3228.437       6748.686
      8         6979.767       3892.011
      9         6971.644       3906.938
     10         7048.447       3880.499
     80         3038.625       7325.875
     81         3050.875       7325.375
```

82	3063.625	7325.125
83	3076.625	7324.875
84	3068.305	7458.467
85	114.685	2604.717
86	97.724	2644.703
87	108.282	2649.420
88	10819.167	1897.465
89	10828.669	1897.259
90	10827.016	1870.199
91	10818.754	1871.025
92	8176.491	5144.866
93	8175.914	5164.483
94	8175.337	5184.965
95	8175.049	5204.293
31	2799.715	2002.352
32	9991.372	1884.385
34	9956.685	1875.620
35	9958.737	1861.820
36	10746.647	2032.269
39	9344.879	5507.190
40	9295.828	5529.829
42	9310.405	5498.638
43	9299.418	5506.310
44	9293.925	5550.921
45	9317.319	5578.482
47	9344.407	5550.352
48	9364.581	5526.484

Affine coefficients from file (pixels) to film (millimeters)

A0	A1	A2	B0	B1	B2
-51.7455	0.009000	0.000000	33.7455	0.000000	-0.009000

image ID = 2

Point ID	x	y
1	4963.514	218.888
2	8685.125	457.375
3	3503.499	5208.096
4	3521.087	5193.573
8	7245.234	2341.094
9	7237.445	2355.884
10	7314.405	2329.346
80	3338.625	5765.125
81	3350.375	5764.875
82	3363.125	5764.125
83	3376.039	5763.904
84	3368.551	5896.662
85	437.621	1093.632
86	421.769	1133.511
87	432.537	1138.496
88	11137.335	296.194
89	11147.579	295.976
90	11146.054	268.731
91	11137.117	269.167
92	8460.622	3591.153
93	8460.373	3611.547
94	8459.627	3631.941
95	8459.378	3651.838
31	3065.930	480.466
32	10289.868	298.470
34	10254.876	289.854
35	10256.458	275.962

36	11065.674	440.724
39	9649.608	3960.206
40	9599.644	3982.872
42	9613.934	3951.435
43	9603.882	3959.418
44	9596.983	4003.962
45	9622.409	4032.344
47	9648.820	4003.568
48	9670.008	3979.029

Affine coefficients from file (pixels) to film (millimeters)

A0	A1	A2	B0	B1	B2
-51.7455	0.009000	0.000000	33.7455	0.000000	-0.009000

THE OUTPUT OF SELF-CALIBRATING BUNDLE BLOCK ADJUSTMENT

the no. of iteration =1 the standard error = 0.1785
the maximal correction of the object points = 1.30783

the no. of iteration =2 the standard error = 0.1785
the maximal correction of the object points = 0.01306

the no. of iteration =3 the standard error = 0.1785
the maximal correction of the object points = 0.00001

The exterior orientation parameters

image ID	Xs	Ys	Zs	OMEGA	PHI	KAPPA
1	173815.9947	444194.4526	2798.3845	-1.2846	2.1211	-172.3726
2	173649.2913	444530.1702	2797.8247	-0.3864	0.6020	-172.7871

The accuracy of the exterior orientation parameters

image ID	mXs	mYs	mZs	mOMEGA	mPHI	mKAPPA
1	0.7492	0.4163	0.1503	0.0085	0.0163	0.0027
2	0.6705	0.3723	0.1376	0.0079	0.0148	0.0018

The interior orientation parameters of photos

image ID	f(mm)	xo(mm)	yo(mm)
1	101.4000	0.0000	0.0000
2	101.4000	0.0000	0.0000

The residuals of the control points

Point ID	rX	rY	rZ
3	-0.0206	-0.0592	0.2189
32	-0.0190	-0.0377	-0.0847
39	-0.0542	-0.0024	-0.1401

aX	aY	aZ
-0.0313	-0.0331	-0.0019

mX	mY	mZ
0.0352	0.0405	0.1578

The residuals of the checkpoints

Point ID	rX	rY	rZ
4	-0.0296	-0.2806	0.3003
8	-0.4029	-0.5328	0.1026
9	-0.4292	-0.9353	0.5581
10	-0.2208	-0.4717	0.0503
31	0.0796	-0.9344	0.4084
2	-0.1975	-0.0593	-0.1618
34	-0.2942	-0.2157	-0.0188
35	-0.0335	-0.3059	-0.0731
36	-0.0987	0.0971	0.2565
1	-0.3159	-1.2787	-0.6902
40	-0.7508	-1.3094	0.0879
42	-0.6638	-0.9617	0.1256
43	-0.5117	-0.2142	-0.4052
44	-0.5665	-0.4407	0.4450
45	-0.1043	-0.8110	-0.7264
47	-0.6309	0.0344	0.1461
48	-0.1965	0.2718	0.9663

aX	aY	aZ
-0.3157	-0.4911	0.0807
mX	mY	mZ
0.3966	0.6745	0.4218

The coordinates of object points

Point ID	X	Y	Z	Overlap
3	173978.1400	445070.5800	11.1500	2
32	172950.3400	443262.7900	7.1100	2
39	172718.7800	444158.9300	7.5800	2
4	173975.5404	445065.4094	11.3803	2
8	173430.0971	444041.5872	8.5326	2
9	173430.4008	444045.8147	8.9181	2
10	173415.6692	444031.7583	8.3303	2
31	174559.9196	444053.6656	11.7984	2
2	173298.1325	443466.3507	7.7582	2
34	172959.2458	443264.5343	7.1412	2
35	172960.2365	443261.1341	7.0069	2
36	172759.5913	443214.3371	7.7065	2
1	174161.8241	443798.9413	9.9998	2
40	172727.8392	444169.2606	7.7779	2
42	172727.7862	444160.6483	7.7756	2
43	172729.1983	444163.4858	7.2648	2
44	172726.3035	444174.3093	8.1450	2
45	172717.3657	444178.0290	6.9436	2
47	172714.4891	444168.8344	7.7561	2
48	172712.5635	444161.2418	8.5763	2
80	173957.9844	445212.0610	12.3105	2
81	173955.3764	445210.8771	11.9657	2
82	173952.5071	445209.1797	12.9687	2
83	173949.6415	445207.8139	13.0093	2
84	173937.7768	445238.4636	12.5058	2
85	175078.5697	444460.6163	21.4611	2
86	175078.3413	444471.1379	20.9204	2
87	175075.8859	444471.1634	20.1572	2
88	172762.2812	443180.4854	21.1488	2
89	172759.9781	443179.3075	20.9665	2
90	172763.0465	443173.1675	20.6333	2
91	172765.2685	443174.6180	21.5456	2
92	173028.6143	444199.4752	17.2607	2
93	173026.3243	444203.9602	16.0189	2
94	173024.4582	444208.6628	16.4032	2

95	173022.2748	444213.0708	15.5568	2

The total object points = 36

The accuracy of object points

Point ID	mX	mY	mZ	mP	Overlap
80	0.0680	0.1962	0.6298	0.6631	2
81	0.0675	0.1959	0.6297	0.6629	2
82	0.0670	0.1953	0.6289	0.6619	2
83	0.0665	0.1950	0.6286	0.6615	2
84	0.0648	0.2024	0.6308	0.6656	2
85	0.4561	0.0825	0.9419	1.0497	2
86	0.4555	0.0830	0.9406	1.0484	2
87	0.4542	0.0829	0.9398	1.0471	2
88	0.2359	0.2891	0.6639	0.7616	2
89	0.2367	0.2897	0.6646	0.7627	2
90	0.2363	0.2917	0.6659	0.7644	2
91	0.2355	0.2910	0.6649	0.7631	2
92	0.1462	0.0601	0.5459	0.5683	2
93	0.1466	0.0595	0.5463	0.5688	2
94	0.1470	0.0590	0.5463	0.5688	2
95	0.1474	0.0586	0.5466	0.5691	2

amX	amY	amZ
0.2020	0.1645	0.6759

The residuals of image points

Point	Image	Vx	Vy
3	1	0.068	-0.051
3	2	-0.091	0.073

Point	Image	Vx	Vy
32	1	0.009	0.046
32	2	0.011	0.001

Point	Image	Vx	Vy
39	1	0.195	-0.002
39	2	-0.189	-0.066

Point	Image	Vx	Vy
4	1	-0.458	0.013
4	2	0.464	-0.016

Point	Image	Vx	Vy
8	1	-0.071	0.002
8	2	0.070	-0.002

Point	Image	Vx	Vy
9	1	0.083	-0.002
9	2	-0.083	0.003

Point	Image	Vx	Vy
10	1	-0.035	0.001
10	2	0.034	-0.001

Point	Image	Vx	Vy
31	1	-0.261	0.007
31	2	0.264	-0.009

Point	Image	Vx	Vy
2	1	0.008	-0.000

2	2	-0.008	0.000

Point	Image	Vx	Vy
34	1	0.256	-0.007
34	2	-0.251	0.008

Point	Image	Vx	Vy
35	1	0.034	-0.001
35	2	-0.033	0.001

Point	Image	Vx	Vy
36	1	0.719	-0.019
36	2	-0.700	0.023

Point	Image	Vx	Vy
1	1	-0.569	0.016
1	2	0.571	-0.020

Point	Image	Vx	Vy
40	1	0.124	-0.003
40	2	-0.122	0.004

Point	Image	Vx	Vy
42	1	-0.068	0.002
42	2	0.067	-0.002

Point	Image	Vx	Vy
43	1	0.473	-0.013
43	2	-0.465	0.015

Point	Image	Vx	Vy
44	1	-0.291	0.008
44	2	0.285	-0.010

Point	Image	Vx	Vy
45	1	0.430	-0.012
45	2	-0.422	0.014

Point	Image	Vx	Vy
47	1	-0.073	0.002
47	2	0.072	-0.002

Point	Image	Vx	Vy
48	1	0.320	-0.009
48	2	-0.314	0.010

Point	Image	Vx	Vy
80	1	0.080	-0.002
80	2	-0.081	0.003

Point	Image	Vx	Vy
81	1	-0.091	0.002
81	2	0.092	-0.003

Point	Image	Vx	Vy
82	1	0.002	-0.000
82	2	-0.002	0.000

Point	Image	Vx	Vy
83	1	0.045	-0.001
83	2	-0.045	0.002

Point	Image	Vx	Vy
84	1	-0.050	0.001
84	2	0.050	-0.002

Point	Image	Vx	Vy
85	1	-0.207	0.006
85	2	0.212	-0.007

Point	Image	Vx	Vy
86	1	-0.027	0.001
86	2	0.028	-0.001

Point	Image	Vx	Vy
87	1	0.191	-0.005
87	2	-0.196	0.007

Point	Image	Vx	Vy
88	1	-0.211	0.006
88	2	0.205	-0.007

Point	Image	Vx	Vy
89	1	0.033	-0.001
89	2	-0.032	0.001

Point	Image	Vx	Vy
90	1	0.182	-0.005
90	2	-0.178	0.006

Point	Image	Vx	Vy
91	1	-0.038	0.001
91	2	0.037	-0.001

Point	Image	Vx	Vy
92	1	-0.044	0.001
92	2	0.043	-0.001

Point	Image	Vx	Vy
93	1	0.058	-0.002
93	2	-0.057	0.002

Point	Image	Vx	Vy
94	1	-0.077	0.002
94	2	0.076	-0.003

Point	Image	Vx	Vy
95	1	-0.117	0.003
95	2	0.116	-0.004

The image residuals of the control points

The image ID = 1

Point ID	Vx	Vy
3	0.068	-0.051
32	0.009	0.046
39	0.195	-0.002

RMSE of 3 points: mx=0.119, my=0.040

The image ID = 2

Point ID	Vx	Vy

```
          3      -0.091       0.073
         32       0.011       0.001
         39      -0.189      -0.066
  RMSE of 3 points: mx=0.121, my=0.057


The image residuals of the checkpoints

           The image ID = 1
   Point ID       Vx          Vy
          4      -0.458       0.013
          8      -0.071       0.002
          9       0.083      -0.002
         10      -0.035       0.001
         31      -0.261       0.007
          2       0.008      -0.000
         34       0.256      -0.007
         35       0.034      -0.001
         36       0.719      -0.019
          1      -0.569       0.016
         40       0.124      -0.003
         42      -0.068       0.002
         43       0.473      -0.013
         44      -0.291       0.008
         45       0.430      -0.012
         47      -0.073       0.002
         48       0.320      -0.009
  RMSE of 17 points: mx=0.327, my=0.009

           The image ID = 2
   Point ID       Vx          Vy
          4       0.464      -0.016
          8       0.070      -0.002
          9      -0.083       0.003
         10       0.034      -0.001
         31       0.264      -0.009
          2      -0.008       0.000
         34      -0.251       0.008
         35      -0.033       0.001
         36      -0.700       0.023
          1       0.571      -0.020
         40      -0.122       0.004
         42       0.067      -0.002
         43      -0.465       0.015
         44       0.285      -0.010
         45      -0.422       0.014
         47       0.072      -0.002
         48      -0.314       0.010
  RMSE of 17 points: mx=0.323, my=0.011
```

Second generation AT report of NIR image layer.

```
      The Triangulation Report With OrthoBASE

      The output image x, y units:     pixels
      The output angle unit:         gons
      The output ground X, Y, Z units: meters

           The Input Image Coordinates
                 image ID = 5
  Point ID            x             y
       26         6824.159      1093.923
```

27	6828.177	1091.780
28	6832.998	1102.226
29	6977.359	1391.349
30	6981.242	1389.608
31	6986.197	1398.580
1	5631.376	2264.075
2	2693.809	3396.329
8	3142.754	1439.793
9	3142.984	1424.433
10	3092.546	1473.036
32	1509.260	4090.067
33	1539.064	4070.579
34	1541.127	4082.043
35	1543.420	4094.652

Affine coefficients from file (pixels) to film (millimeters)

A0	A1	A2	B0	B1	B2
-39.4560	0.009000	0.000000	20.0700	0.000000	-0.009000

image ID = 6

Point ID	x	y
26	6824.397	1093.117
27	6827.944	1091.207
28	6832.991	1101.439
29	6978.009	1391.475
30	6981.693	1389.428
31	6986.058	1397.886
1	5630.556	2264.038
2	2693.226	3396.761
8	3142.736	1439.241
9	3142.532	1424.767
10	3092.585	1473.287
32	1509.167	4090.912
33	1538.523	4070.933
34	1541.785	4081.738
35	1543.212	4094.377

Affine coefficients from file (pixels) to film (millimeters)

A0	A1	A2	B0	B1	B2
-39.4515	0.009000	0.000000	20.0700	0.000000	-0.009000

THE OUTPUT OF SELF-CALIBRATING BUNDLE BLOCK ADJUSTMENT

the no. of iteration =1 the standard error = 3.5996
the maximal correction of the object points =3393.62560

the no. of iteration =2 the standard error = 0.5154
the maximal correction of the object points =3180.49011

the no. of iteration =3 the standard error = 0.4287
the maximal correction of the object points =1927.63905

the no. of iteration =4 the standard error = 0.8742
the maximal correction of the object points = 672.76588

the no. of iteration =5 the standard error = 2.0855
the maximal correction of the object points = 301.84426

Warning: The iteration cannot be converged! There are probably errors in your data!

The exterior orientation parameters

image ID	Xs	Ys	Zs	OMEGA	PHI	KAPPA
5	174197.6435	444744.8244	3283.2429	-17.8704	7.6706	2.0046
6	174205.1694	444741.2182	3282.6560	-17.8094	7.8099	2.0052

The interior orientation parameters of photos

image ID	f(mm)	xo(mm)	yo(mm)
5	101.4000	0.0000	0.0000
6	101.4000	0.0000	0.0000

The residuals of the control points

Point ID	rX	rY	rZ
1	0.7800	1.7889	12.0027
28	-1.4219	3.9943	19.3770
8	-42.0614	-21.0824	
31	-8.0743	10.4005	
35	-46.6070	-40.3520	

aX	aY	aZ
-19.4769	-9.0501	15.6898

mX	mY	mZ
28.3168	20.9765	16.1173

The residuals of the checkpoints

Point ID	rX	rY	rZ
2	-39.4951	-42.8543	8.2912
9	-42.2482	-21.0150	-75.9060
32	-70.6807	-67.8728	22.6789
10	-54.9492	-32.1228	-257.7444

aX	aY	aZ
-51.8433	-40.9662	-75.6701

mX	mY	mZ
53.2915	44.4879	134.8860

The coordinates of object points

Point ID	X	Y	Z	Overlap
1	174162.1400	443800.2200	-4.3891	2
28	174509.1341	444138.3860	-121.0211	2
8	173430.5000	444042.1200	-67.4543	2
31	174559.8400	444054.6000	-45.6017	2
35	172960.2700	443261.4400	198.6070	2
2	173258.8349	443423.5557	80.1336	2
9	173388.5818	444025.7350	-67.5460	2
32	172879.6593	443194.9172	144.0131	2
10	173360.9408	444000.1072	-112.7207	2
26	174507.4877	444139.9842	-129.0720	2
27	174505.0094	444147.5985	-89.5452	2
29	174563.1121	444039.9680	-178.6431	2
30	174560.0808	444048.5821	-139.2263	2
33	172916.5681	443233.5527	207.6211	2
34	172874.8733	443179.9971	106.3920	2

The total object points = 15

The residuals of image points

Point	Image	Vx	Vy
1	5	-2.044	-5.328
1	6	-1.917	-5.374

Point	Image	Vx	Vy
28	5	-1.287	1.745
28	6	-1.177	1.880

Point	Image	Vx	Vy
8	5	131.120	-64.080
8	6	130.735	-63.551

Point	Image	Vx	Vy
31	5	25.795	35.259
31	6	25.855	35.257

Point	Image	Vx	Vy
35	5	134.889	-111.173
35	6	134.849	-111.467

Point	Image	Vx	Vy
2	5	-0.108	0.251
2	6	0.108	-0.251

Point	Image	Vx	Vy
9	5	-0.075	0.165
9	6	0.075	-0.165

Point	Image	Vx	Vy
32	5	-0.241	0.624
32	6	0.241	-0.624

Point	Image	Vx	Vy
10	5	-0.019	0.040
10	6	0.019	-0.040

Point	Image	Vx	Vy
26	5	0.044	-0.088
26	6	-0.044	0.088

Point	Image	Vx	Vy
27	5	-0.048	0.100
27	6	0.047	-0.100

Point	Image	Vx	Vy
29	5	-0.089	0.192
29	6	0.089	-0.191

Point	Image	Vx	Vy
30	5	-0.051	0.107
30	6	0.051	-0.107

Point	Image	Vx	Vy
33	5	-0.195	0.488
33	6	0.195	-0.488

Point	Image	Vx	Vy
34	5	0.009	-0.019
34	6	-0.009	0.019

```
The image residuals of the control points

            The image ID = 5
    Point ID       Vx          Vy
          1      -2.044      -5.328
         28      -1.287       1.745
          8     131.120     -64.080
         31      25.795      35.259
         35     134.889    -111.173
  RMSE of 5 points: mx=84.922, my=59.565

            The image ID = 6
    Point ID       Vx          Vy
          1      -1.917      -5.374
         28      -1.177       1.880
          8     130.735     -63.551
         31      25.855      35.257
         35     134.849    -111.467
  RMSE of 5 points: mx=84.793, my=59.563


The image residuals of the checkpoints

            The image ID = 5
    Point ID       Vx          Vy
          2      -0.108       0.251
          9      -0.075       0.165
         32      -0.241       0.624
         10      -0.019       0.040
  RMSE of 4 points: mx=0.138, my=0.347

            The image ID = 6
    Point ID       Vx          Vy
          2       0.108      -0.251
          9       0.075      -0.165
         32       0.241      -0.624
         10       0.019      -0.040
  RMSE of 4 points: mx=0.138, my=0.347
```

E. Sensitivity analysis classification.

The results of the sensitivity analysis are “DTM Point Status Images” representing a correlation between the block checkpoints heights and the generated DSM cell heights. No other detailed information concerning the correlation is found.
The correlation results are categorized according to the following criteria.
Points considered Excellent have a correlation value between 1 and 0.85.
Good points have a correlation value between 0.85 and 0.7.
Fair points have a correlation value between 0.7 and 0.5.
Isolated points do not have any immediate neighbours.
Suspicious points are found using the following technique.
1. A 3 x 3 window is used to calculate an elevation value using the neighbouring DTM postings.
2. The known (that is, extracted) elevation value is subtracted from the interpolated value to compute the difference.
3. The standard deviation of the neighbouring DTM postings is captured.

4. If the difference is three times larger than the standard deviation, the interpolated elevation value is used and the point is considered Suspicious. (Adapted from Erdas Imagine Help manual).

The following graphs are the results of the method described in 3.1.4 to establish the expert DSM generation settings.

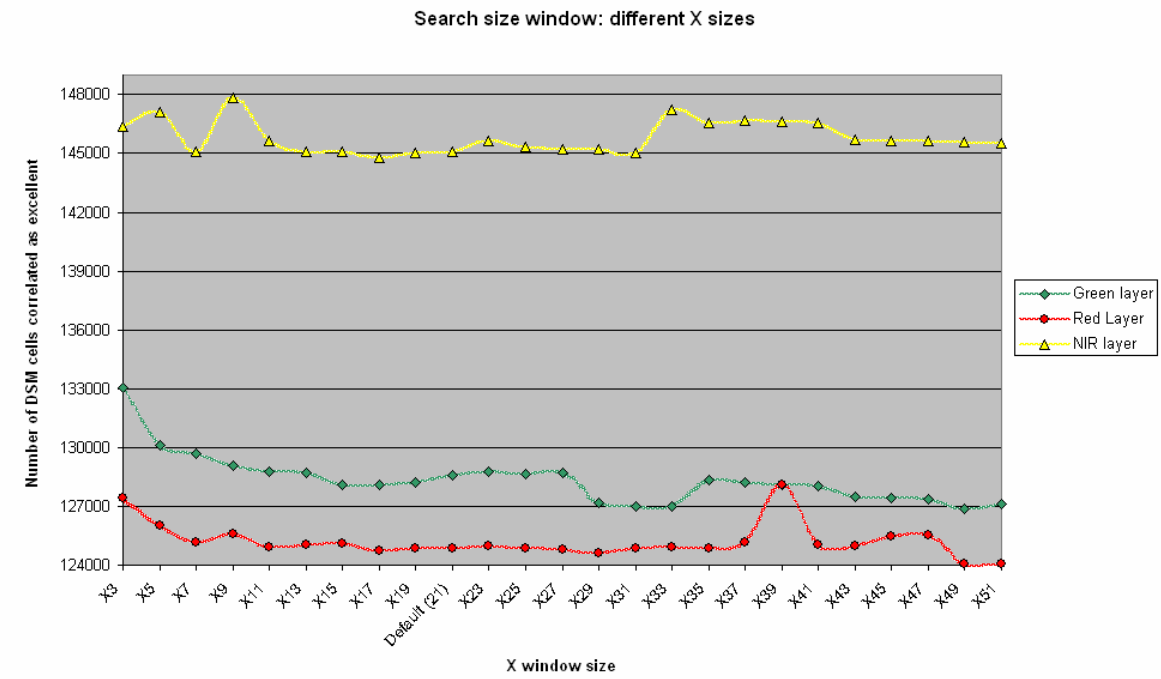

Fig. 26: Results of the search window size analysis (X).

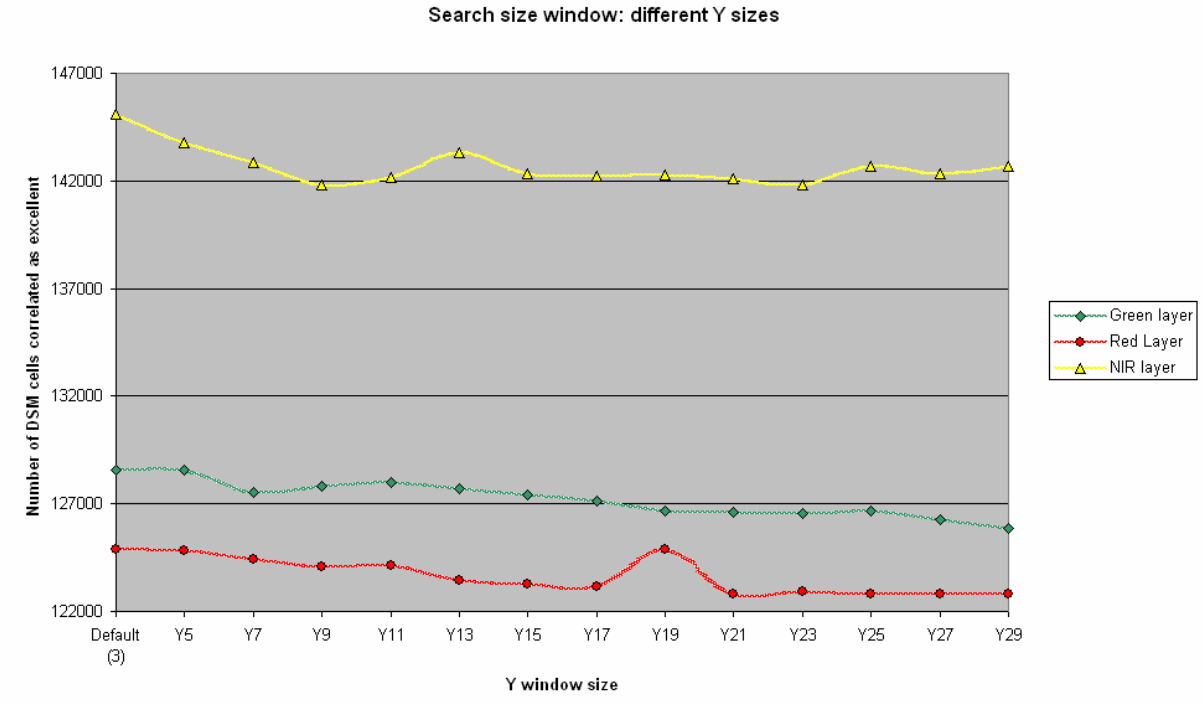

Fig. 27: Results of the search window size analysis (Y).

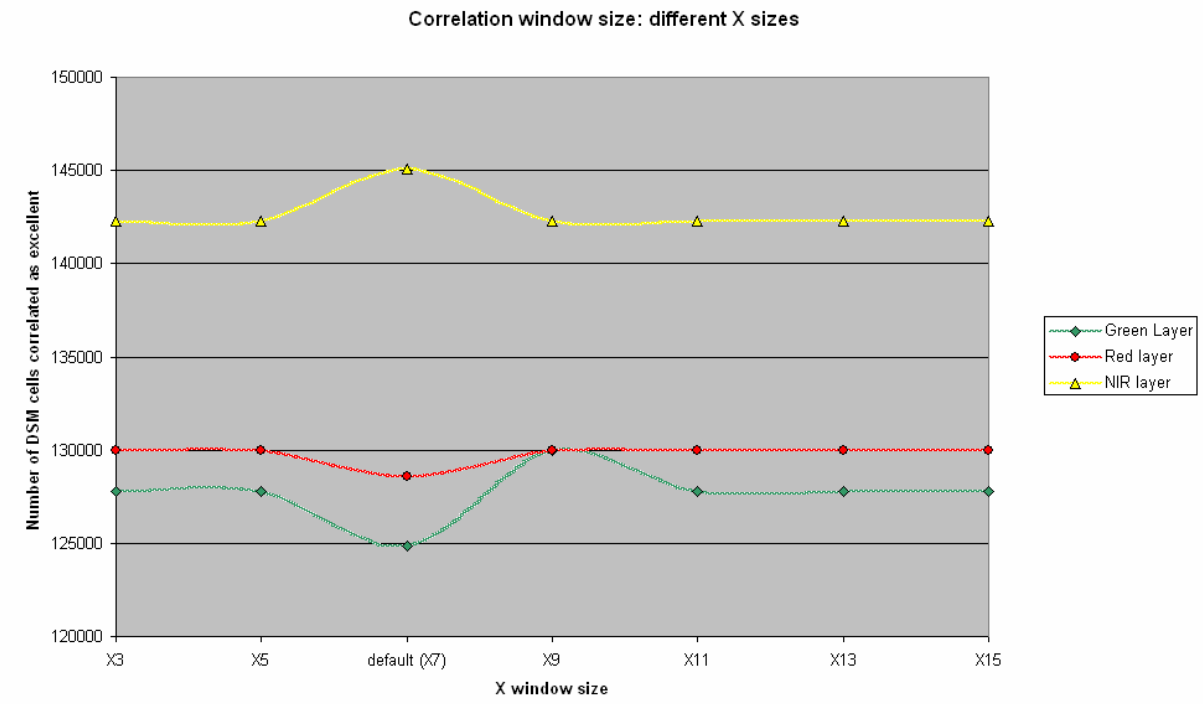

Fig. 28: Results of the correlation window size analysis (X).

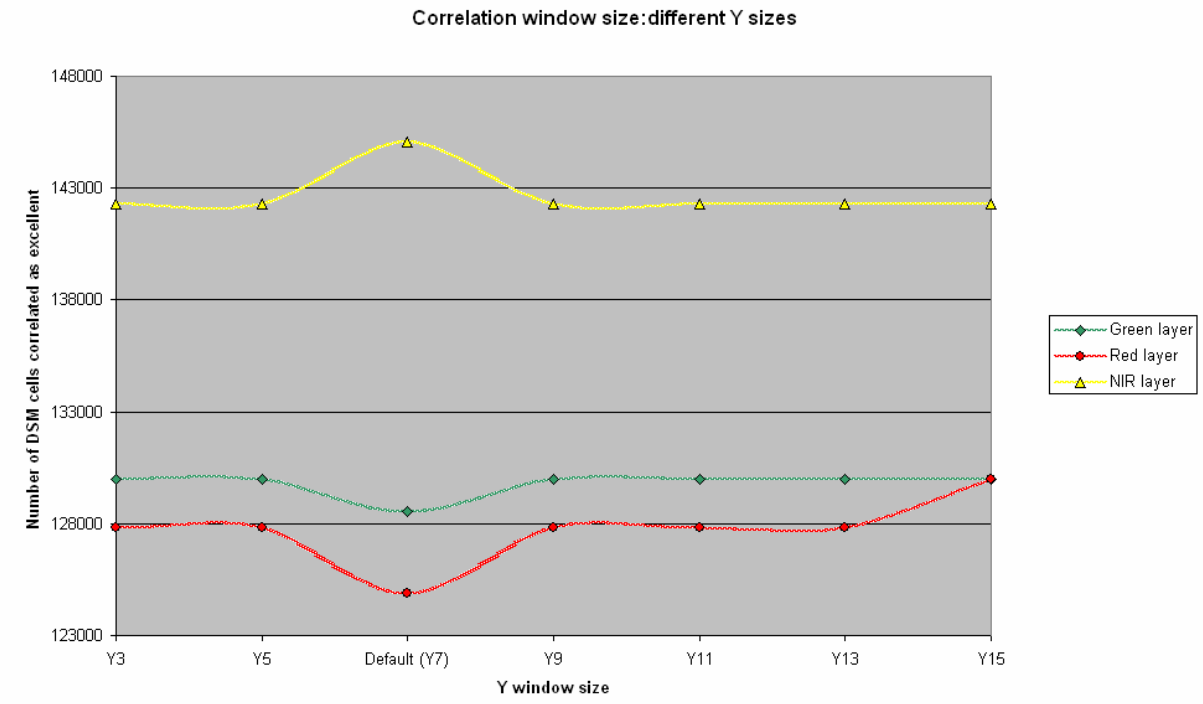

Fig. 29: Results of the correlation window size analysis (Y).

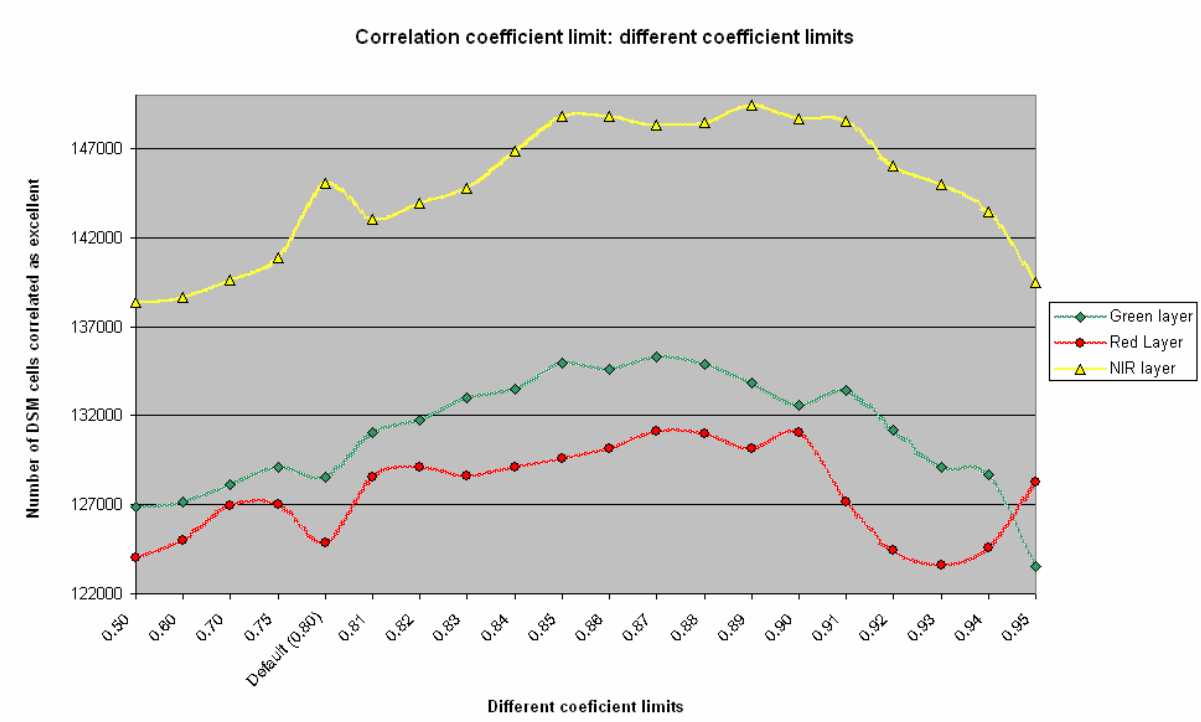

Fig. 30: Results of the correlation coefficient analysis.

The following graphs present the results of the sensitivity analysis classification summarized in table 7.

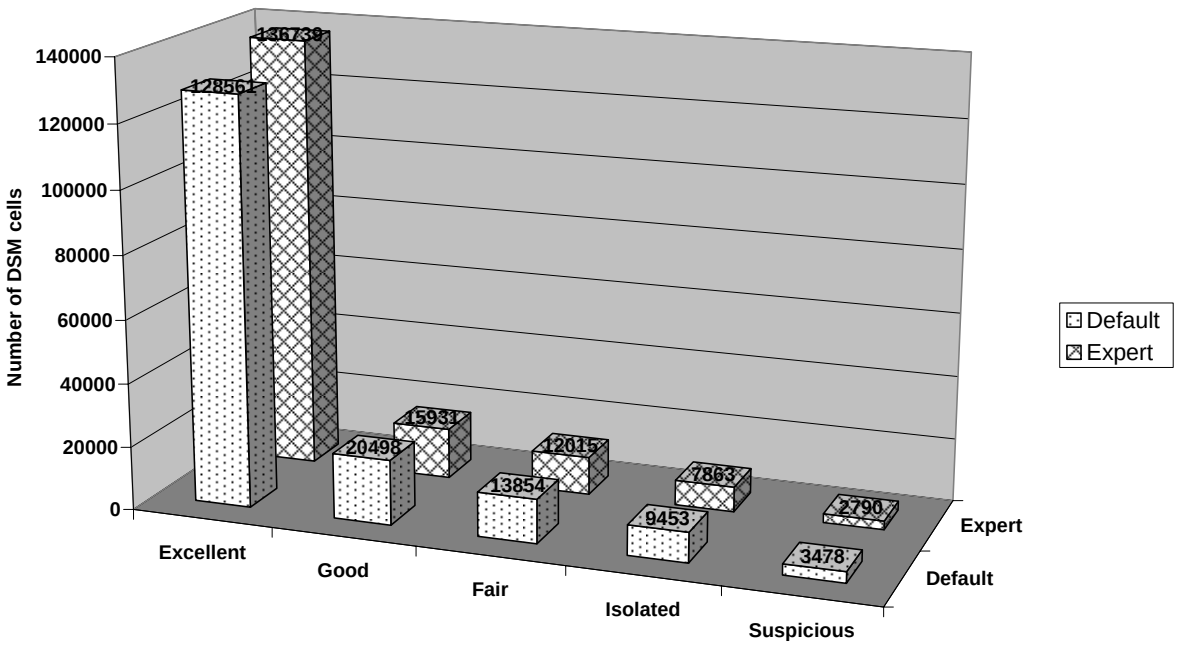

Fig. 31: Classification of default and expert DSM generation settings using the green image layer.

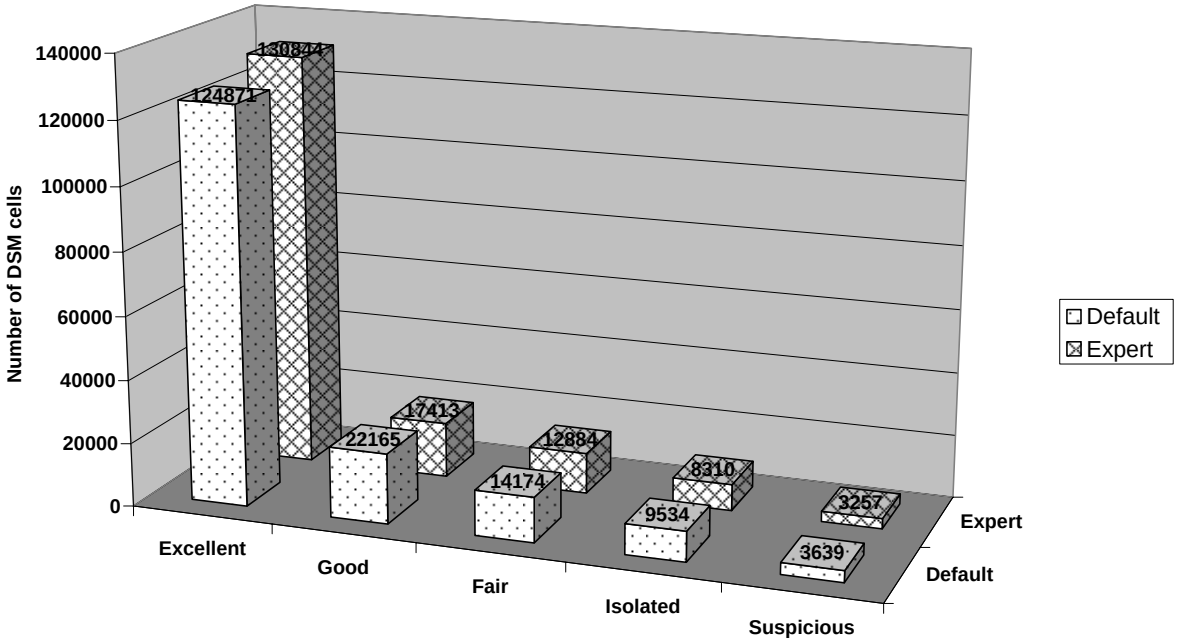

Fig. 32: Classification of default and expert DSM generation settings using the red image layer.

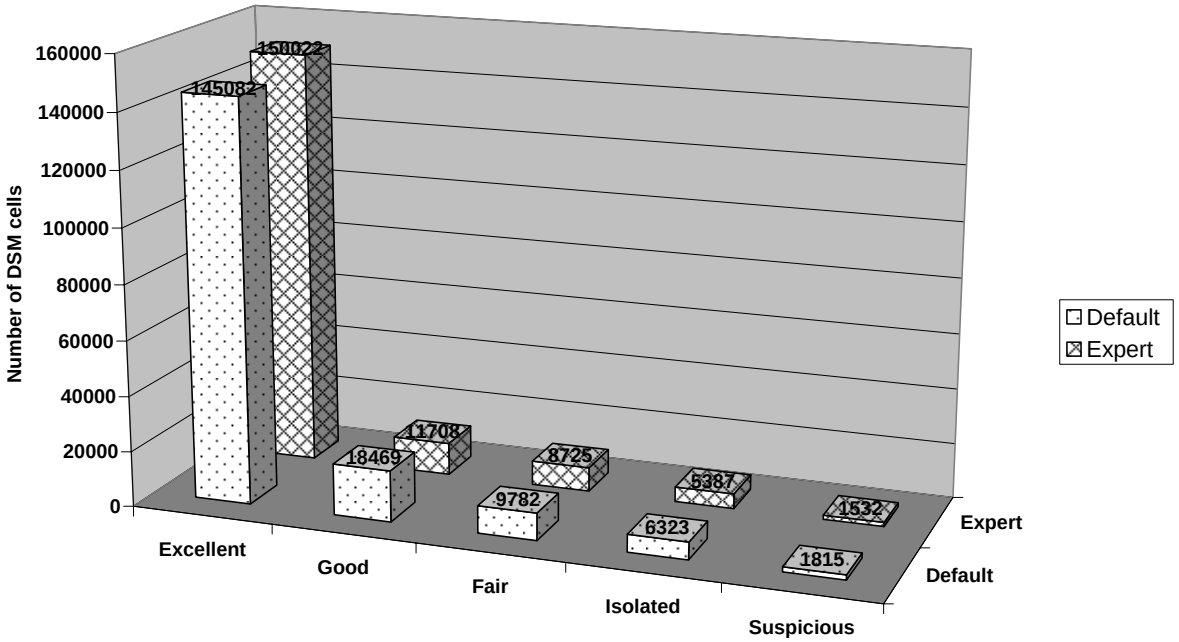

Fig. 33: Classification of default and expert DSM generation settings using the NIR image layer.

F. Internal validation classification check.

Here is the result of checking the internal validation process (i.e. “DTM Point Status Output Image”) by means of creating a so called “quality image” of the expert NIR DSM, using only the GCP’s in the first trial, the checkpoints in the second trial and the tie points in the third trial. A combination of GCP’s and checkpoint was also tested and finally a combination of all points was checked.

Table 17: Result of using different block points for the internal validation classification.

Points used	GCP's	Checkpoints	Tie points	GCP's and checkpoints	All points
Points classification result					
Excellent	150022	150022	150022	150022	150022
Good	11708	11708	11708	11708	11708
Fair	8725	8725	8725	8725	8725
Isolated	5387	5387	5387	5387	5387
Suspicious	1532	1532	1532	1532	1532

G. Field measurements.

Presented here are the results of forestry measurements in the study area and volume estimation via SPSS module.

Table 18: Study area sampling plot 1 data.

				Height (m)	Height 2 (m)		
Tree nr.	Species	Dead/Alive	DBH (cm)	1	2	Average H	V (m3)
1	QR	A	36.7	28.1	25.4	26.8	1.3
2	QR	A	42.5	26.9	25.9	26.4	1.7
3	BP	D	23.3	4.0	4.2	4.1	0.1
4	BP	A	37.3	23.7	26.0	24.9	1.0
5	QR	A	20.2	20.7	20.4	20.6	0.3
6	Alnus	A	18.5	19.7	21.3	20.5	0.3
7	Alnus	A	12.5	15.3	14.6	15.0	0.1
8	QR	A	28.8	22.2	24.3	23.3	0.7
9	Alnus	A	16.6	7.9	8.1	8.0	0.1
10	BP	A	34.2	26.0	27.6	26.8	1.0
11	QR	A	16.3	15.0	16.8	15.9	0.2
12	BP	D	14.9	6.0	5.9	6.0	0.0
13	BP	A	18.0	21.8	21.5	21.7	0.3
14	Alnus	A	21.3	21.1	22.9	22.0	0.4
15	QR	A	8.8	8.3	8.1	8.2	0.0
16	BP	A	25.2	23.5	25.0	24.3	0.5
17	QR	A	33.9	27.9	23.6	25.8	1.1
18	BP	A	27.1	23.9	24.7	24.3	0.6
19	BP	A	24.1	22.9	21.6	22.3	0.4
20	BP	A	34.6	22.4	21.4	21.9	0.8
21	Alnus	A	20.1	22.6	22.8	22.7	0.3

QR = Quercus Robur (Oak).
BP = Betula Pendula (Birch).
Alnus = Alnus glutinosa (Alder).

Table 19: Study area sampling plot 2 data.

				Height (m)	Height 2 (m)		
Tree nr.	Specie	Dead/Alive	DBH (cm)	1	2	Average H	V (m3)
1	Alnus	A	17.5	21.7	21.8	21.8	0.2
2	QR	A	20.4	16.8	17.9	17.4	0.3
3	QR	A	43.8	27.1	26.7	26.9	1.8
4	QR	A	25.8	20.7	19.4	20.1	0.5
5	QR	D	26.6	23.0	24.7	23.9	0.7
6	QR	A	17.4	11.1	11.5	11.3	0.1
7	QR	A	33.5	22.7	23.9	23.3	1.0
8	QR	A	33.2	24.0	25.1	24.6	1.0
9	BP	A	24.4	24.4	26.7	25.6	0.5
10	QR	A	17.8	15.8	19.1	17.5	0.2
11	QR	D	9.1	8.2	8.2	8.2	0.0
12	QR	D	17.9	4.9	5.1	5.0	0.1
13	Alnus	A	27.5	20.3	22.2	21.3	0.6
14	QR	A	19.0	17.4	19.5	18.5	0.3
15	QR	A	34.0	22.2	23.7	23.0	1.0
16	BP	A	17.4	19.4	21.3	20.4	0.2
17	BP	A	17.7	19.5	20.2	19.9	0.2
18	BP	A	22.4	21.7	23.6	22.7	0.4
19	QR	A	31.8	25.5	24.8	25.2	1.0
20	QR	A	36.2	28.1	25.1	26.6	1.3
21	QR	D	21.4	11.5	11.6	11.6	0.2

QR = Quercus Robur (Oak).
BP = Betula Pendula (Birch).
Alnus = Alnus glutinosa (Alder).

Table 20: Study area sampling plot 3 data.

				Height (m)	Height 2 (m)		
Tree nr.	Specie	Dead/Alive	DBH (cm)	1	2	Average H	V (m3)
1	QR	A	29.4	23.5	24.4	24.0	0.8
2	QR	A	34.9	26.4	27.8	27.1	1.2
3	QR	A	32.3	24.2	25.5	24.9	1.0
4	QR	A	14.3	15.4	17.5	16.5	0.1
5	QR	A	28.4	24.8	24.9	24.9	0.8
6	QR	D	15.8	18.0	17.8	17.9	0.2
7	QR	A	37.5	24.7	26.5	25.6	1.3
8	QR	D	20.9	19.8	18.9	19.4	0.3
9	QR	A	23.2	23.5	22.7	23.1	0.5
10	QR	A	13.4	14.1	14.8	14.5	0.1
11	QR	A	30.2	23.6	23.7	23.7	0.8
12	QR	D	11.2	9.3	9.6	9.5	0.0
13	QR	A	19.0	20.2	18.2	19.2	0.3
14	QR	A	37.4	24.9	26.4	25.7	1.3
15	QR	A	35.4	26.4	26.7	26.6	1.2
16	QR	A	21.8	22.9	21.5	22.2	0.4
17	QR	A	31.5	23.7	25.5	24.6	0.9
18	BP	D	24.7	9.9	9.7	9.8	0.2
19	BP	A	32.2	23.0	22.4	22.7	0.7
20	QR	A	38.5	26.4	25.7	26.1	1.4
21	QR	D	16.7	19.3	20.0	19.7	0.2

QR = Quercus Robur (Oak).
BP = Betula Pendula (Birch).
Alnus = Alnus glutinosa (Alder).

H. DSM and image segmentation trials.

The following images present segmentation trial preformed using the eCognition software. All segmentation trials were done with default segmentation settings on the NIR image layer. Three segmentation ´scales´ (i.e. 10, 25 and 50) were tested with the inclusion or exclusion of the DSM or image in the segmentation process.

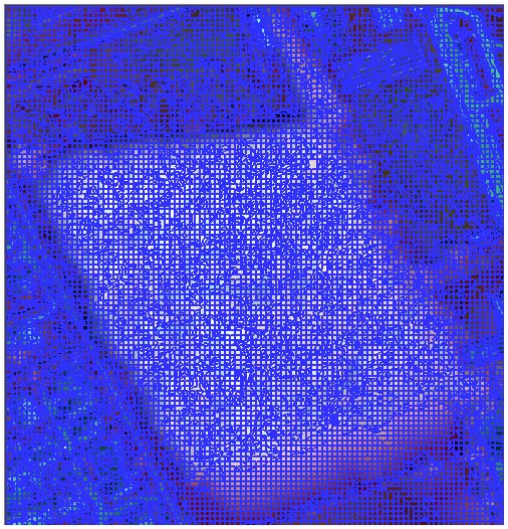

Fig. 34: Image and DSM segmentation scale 10.

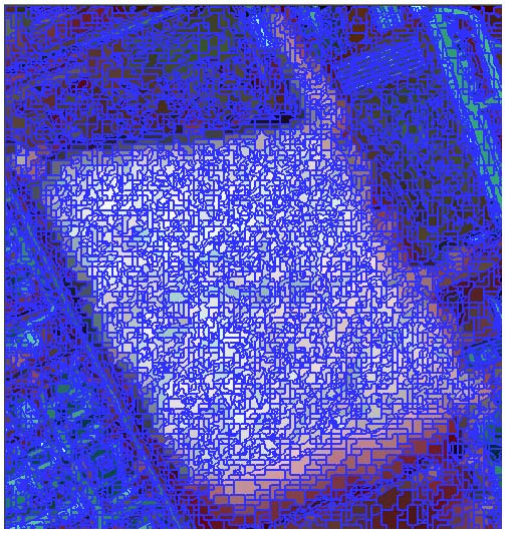

Fig. 35: Image segmentation scale 10.

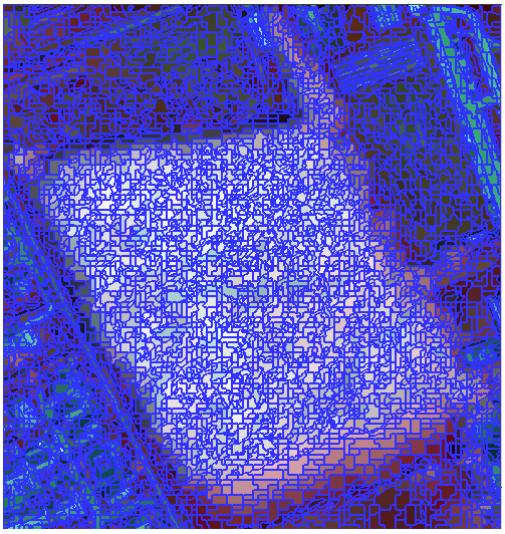

Fig. 36: DSM segmentation scale 10.

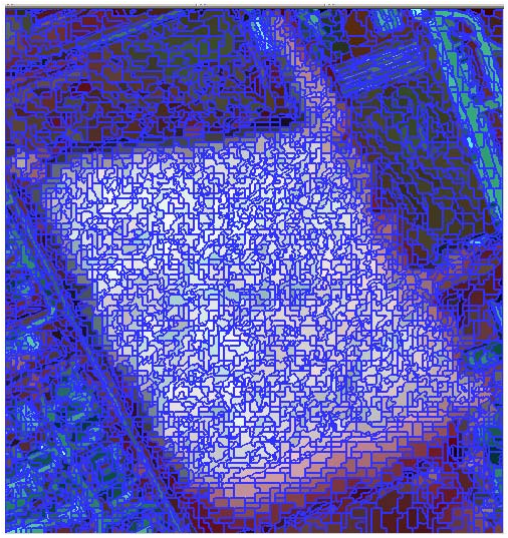

Fig. 37: Image and NIR DSM segmentation scale 25.

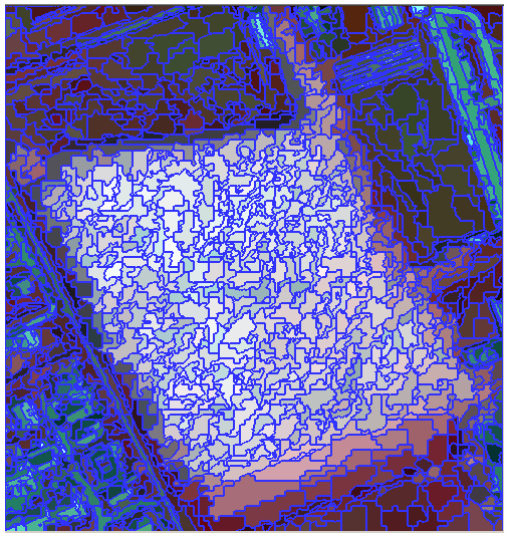

Fig. 38: Image segmentation scale 25.

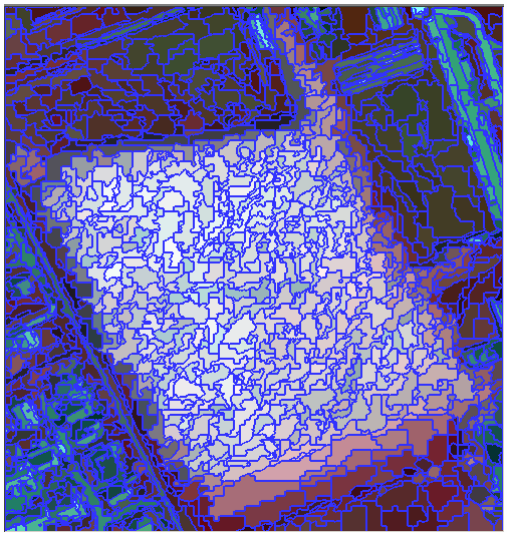

Fig. 39: NIR DSM segmentation scale 25.

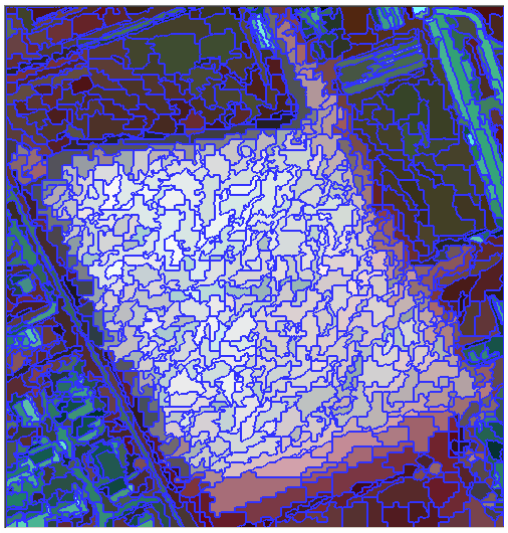

Fig. 40: Image and NIR DSM segmentation scale 50.

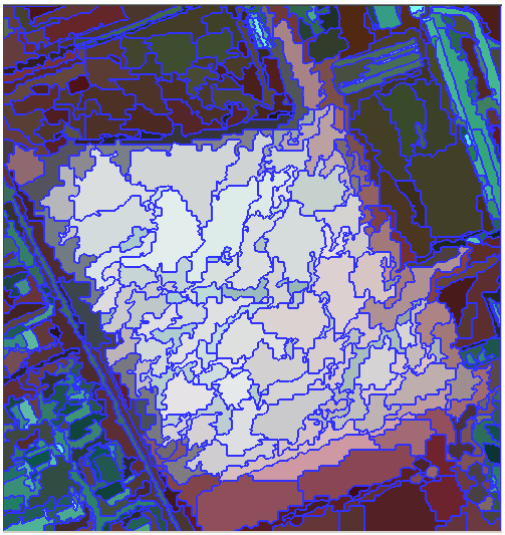

Fig. 41: Image segmentation scale 50.

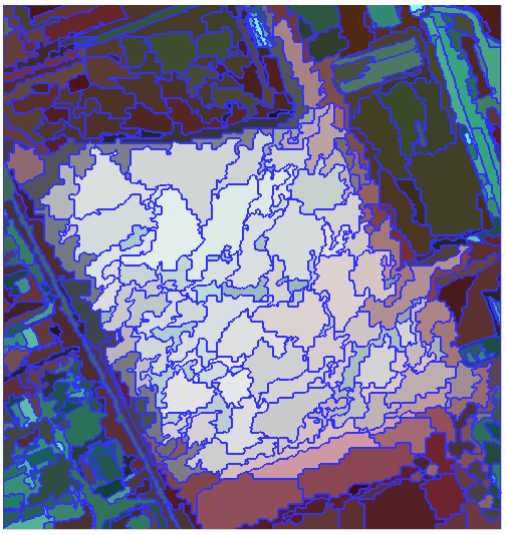

Fig. 42: NIR DSM segmentation scale 50.

I. Automatic tie point generation trial.

Table 21 present the results of automatically generating tie points, to investigate if this feature could be used as an indicator for appropriate image layer selection. In all trials, the default TPG settings were used, with the option to Keep All (KA*) tie points generated.

Table 21: Automatic tie point generation trials results.

Image layer	Green	Red	NIR
Default KA*	1133	1324	824

Detailed information regarding the TPG properties can be found in the TPG properties help.

J. Orthoimages generation settings.

Table 22 present the settings used in the orthoimages generation.

Table 22: Orthoimages generation settings.

Input image name	Output image name	Active area	Resample method	DTM source	DTM	Z units	DTM overlap
cir_00234.img	1gen_defortho34_nir.img	100	bilinear	DEM	1gen_defdsm_nir.img	centimeters	30
cir_00233.img	1gen_deforhto33_nir.img	100	bilinear	DEM	1gen_defdsm_nir.img	centimeters	30
cir_00233.img	1gen_exporhto33_nir.img	100	bilinear	DEM	1gen_expdsm_nir.img	centimeters	30
cir_00234.img	1gen_exportho34_nir.img	100	bilinear	DEM	1gen_expdsm_nir.img	centimeters	30

Input image name	Output image name	ULX	ULY	LRX	LRY	Cell X	Cell Y	Ignore value
cir_00234.img	1gen_defortho34_nir.img	172509	444465	175104	443160	0.293	0.293	0
cir_00233.img	1gen_deforhto33_nir.img	172509	444465	175104	443160	0.293	0.293	0
cir_00233.img	1gen_exporhto33_nir.img	172507	444465	175084	443154	0.294	0.294	0
cir_00234.img	1gen_exportho34_nir.img	172507	444465	175083	443154	0.294	0.294	0